Journal Pre-proof

Chelating agent effects in the synthesis of supported Ni nanoparticles as catalysts for hydrogen production

Alejandra C. VillagrannullOlivares (Investigation) (Formal analysis) (Writing - original draft) (Visualization), Mariana N. Barroso (Conceptualization) (Validation), Carlos A. López (Formal analysis) (Validation), Jordi Llorca (Validation), María C. Abello (Conceptualization) (Validation) (Visualization) (Writing - review and editing)

Please cite this article as: Villagranx2d7;Olivares AC, Barroso MN, Loacute;pez CA, Llorca J, Abello MC, Chelating agent effects in the synthesis of supported Ni nanoparticles as catalysts for hydrogen production, *Applied Catalysis A, General* (2021), doi: https://doi.org/10.1016/j.apcata.2021.118219

This is a PDF file of an article that has undergone enhancements after acceptance, such as the addition of a cover page and metadata, and formatting for readability, but it is not yet the definitive version of record. This version will undergo additional copyediting, typesetting and review before it is published in its final form, but we are providing this version to give early visibility of the article. Please note that, during the production process, errors may be discovered which could affect the content, and all legal disclaimers that apply to the journal pertain.

Chelating agent effects in the synthesis of supported Ni nanoparticles as catalysts for hydrogen production

Alejandra C. Villagran-Olivares[a*], Mariana N. Barroso[a], Carlos A. López[a], Jordi Llorca[b], María C. Abello[a]

[a] Instituto de Investigaciones en Tecnología Química (INTEQUI-CONICET-UNSL), Facultad de Química, Bioquímica y Farmacia. Almirante Brown 1455, 5700, San Luis, Argentina.
[b] Instituto de Técnicas Energéticas, Departamento de Ingeniería Química, Universitat Politècnica de Catalunya, EEBE, 08019, Barcelona, España.

Graphical Abstract
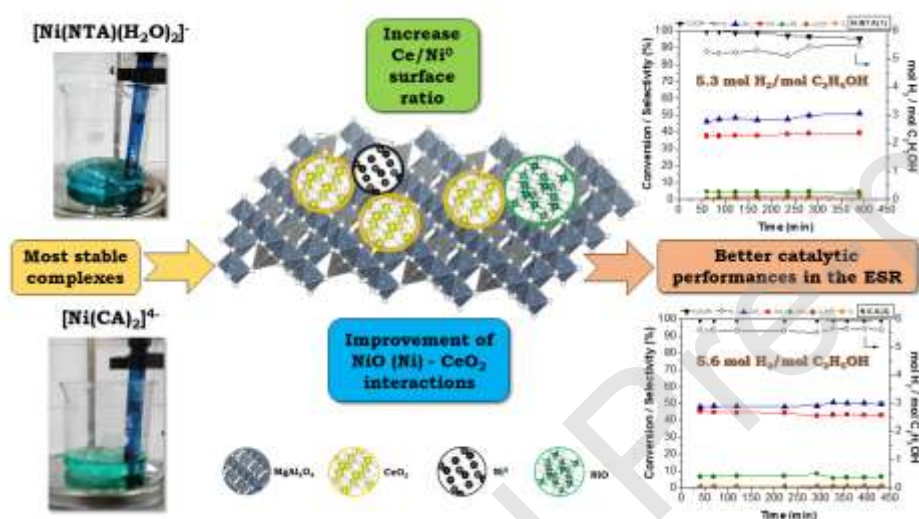
Highlights

- Ni/MgAl$_2$O$_4$-CeO$_2$ were prepared using NTA or CA with different chelate/Ni ratios
- The use of NTA or CA modifies Ni-CeO$_2$ interactions
- All the catalysts prepared with NTA or CA showed a decrease in NiO crystallite size
- The use of NTA also shows a decrease in CeO$_2$ crystallite size
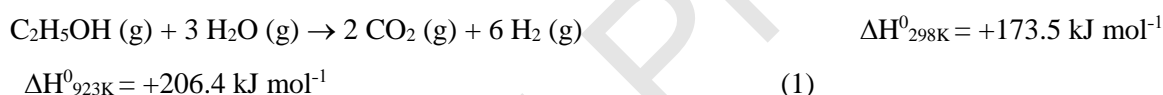- The best performances were obtained for the catalysts prepared from the most stable nickel complex

Abstract

A series of Ni supported over $MgAl_2O_4$-CeO_2 catalysts have been prepared by the wet impregnation method as catalysts for steam ethanol reforming. The synthesis was performed using nitrilotriacetic acid (NTA) or citric acid (CA) as chelating agents (L) with different L/Ni molar ratios. The features of catalytic solids were determined by DR-UV-Vis-NIR, FTIR, BET, TGA, XRD, H_2-TPR, XPS, Raman, HRTEM and SEM. Changes in the crystallite size of NiO and CeO_2 were evidenced with the use of NTA, while the addition of CA allowed to reduce the crystallite size of NiO and Ni with a slight effect in CeO_2 size. The use of chelating agents induced changes in the Ni-CeO_2 interactions and an increase in the Ce/Ni^0 surface ratio. Catalytic systems prepared using an L/Ni ratio leading to the most stable complex formation (NTA/Ni=1 and CA/Ni=2) exhibited the best performances in the reforming reaction under the operation conditions studied.

Keywords: Nano-Ni catalysts, Chelating agent, Complexing method, Hydrogen, Ethanol steam reforming

1. Introduction

Ethanol steam reforming (ESR) is a potential sustainable hydrogen production process, and it has been extensively studied over non-noble transition metal catalysts because they are less expensive than the noble metal ones. In particular, Ni catalysts are preferred because Ni dissociates C-C bonds more efficiently than Co [1-3]. ESR is an endothermic process, which produces 6 mol of hydrogen and 2 mol of carbon dioxide if only the reforming reaction occurs (equation 1). However, other reactions usually occur such as ethanol dehydrogenation, acetaldehyde steam reforming, ethanol dehydration, ethanol decomposition, acetaldehyde decomposition, water gas shift reaction, ethylene decomposition, methane decomposition and Boudouard reaction (equations 2-10) [1]:

$$C_2H_5OH\ (g) + 3\ H_2O\ (g) \rightarrow 2\ CO_2\ (g) + 6\ H_2\ (g) \qquad \Delta H^0_{298K} = +173.5\ kJ\ mol^{-1}$$
$$\Delta H^0_{923K} = +206.4\ kJ\ mol^{-1} \qquad\qquad (1)$$

$$C_2H_5OH\ (g) \rightarrow C_2H_4O\ (g) + H_2\ (g) \qquad \Delta H^0_{298K} = +68.9\ kJ\ mol^{-1} \qquad (2)$$

$$C_2H_4O\ (g) + H_2O\ (g) \rightarrow 2\ CO\ (g) + 3\ H_2\ (g) \qquad \Delta H^0_{923K} = +186.8\ kJ\ mol^{-1} \qquad (3)$$

$$C_2H_5OH\ (g) \rightarrow C_2H_4\ (g) + H_2O\ (g) \qquad \Delta H^0_{298K} = +45.5\ kJ\ mol^{-1} \qquad (4)$$

$$C_2H_5OH\ (g) \rightarrow CO\ (g) + CH_4\ (g) + H_2\ (g) \qquad \Delta H^0_{298K} = +49.6\ kJ\ mol^{-1} \qquad (5)$$

$$C_2H_4O\ (g) \rightarrow CH_4\ (g) + CO\ (g) \qquad \Delta H^0_{298K} = -19.3\ kJ\ mol^{-1} \qquad (6)$$

$$CO\ (g) + H_2O\ (g) \leftrightarrow CO_2\ (g) + H_2\ (g) \qquad \Delta H^0_{298K} = -41.4\ kJ\ mol^{-1} \qquad (7)$$

$$C_2H_4\ (g) \rightarrow 2\ C\ (s) + 2\ H_2\ (g) \qquad \Delta H^0_{298K} = -52.3\ kJ\ mol^{-1} \qquad (8)$$

$$CH_4 (g) \rightarrow 2\ H_2 (g)\ + C (s) \qquad\qquad \Delta H^0_{298K} = +74.9\ kJ\ mol^{-1} \qquad\qquad (9)$$

$$2\ CO (g)\ \leftrightarrow CO_2 (g)\ + C (s) \qquad\qquad \Delta H^0_{298K} = -\ 172.6\ kJ\ mol^{-1} \qquad\qquad (10)$$

The occurrence of these reactions mainly depends on the properties of catalyst and operation conditions. One of the disadvantages of the secondary reactions over Ni catalysts is the deactivation by carbon deposition, sintering and active phase oxidation [4]. Ethylene decomposition, Boudouard reaction and methane decomposition are the main routes to carbon deposition [1-3, 5]. However, there is no linear relationship between the decrease in catalyst activity and coke content [5]. These phenomena of deactivation are the main technological obstacles in today's reformers. The development of a Ni stable catalyst could be achieved by metallic particles below a critical size. As in the methane reforming the control of metal assembly size in the ESR has the same objective: to increase dispersion and decrease carbon deposition by inhibiting its formation reactions. Small particles decrease carbon deposition rate [6], however, they are more susceptible to sintering and oxidation. The method variation of the active phase incorporation in a catalyst could result in different physicochemical properties, allowing low carbon amounts and increasing the stability of Ni catalysts [7,8]. In addition, the characteristics of the precursor species of the active phase often affect the catalyst surface properties and its catalytic behaviour. The choice of a precursor is a very important step in catalyst preparation. Aqueous solutions containing chelating agents in the wet impregnation method has been reported as a strategy to promote smaller active phase particles [9]. Van Dillen et al. [9] have pointed out that the use of aqueous solutions of chelating agents in the conventional wet impregnation method is very attractive, since it retains the simplicity of the technique and it allows to obtain uniform distributions of the active phase and, in general, greater dispersions. A characteristic of these solutions is that, during the solvent remotion, the viscosity of metal complex solutions increases substantially due to a gelling process, affecting the drying stage, inhibiting the redistribution of surface species and favoring the formation of poorly crystallized compounds with high dispersion. In literature, the use of chelating agent has been reported mainly in the synthesis of hydrodesulfurization catalysts [10-12], catalysts for Fischer-Tropsch synthesis [13,14] and recently, for reforming catalysts [15-17].

The incorporation of chelating agents into a transition metal solution generates metal complexes that are charged. In the catalysts preparation by using these impregnation solutions it is necessary to take into account factors such as: chelating agent/metal ratio, pH of impregnation solution and the point of zero charge (PZC) of support [18]. Some published works on ESR have reported important improvements in catalytic properties by using citric acid (CA) [19,20]. Nitrilotriacetic acid, NTA, and CA are chelating agents with the same amount of carbon atoms. NTA have carboxylates and nitrogen groups, while CA has carboxylate groups and a hydroxyl group. The donor capacity of a chelating agent is given by the amount of binding sites presents in its structure, both functional groups and coordination sites, as well as the pair of free electrons of the nitrogen atom in NTA or oxygen atom in CA. The greater the electron-giving capacity of a chelating agent, the greater

the bond strength with the central ion [21] and consequently more stable the complex formed will be. NTA and CA acids have the same amount of functional groups and coordination sites. However, NTA forms complexes more stable with nickel and cerium than CA [22,23], then it is interesting to compare the behaviour of both acids.

On the other hand, in the literature it has been reported the modification of acid/base properties of supports by addition of modifiers such as alkaline metals (Na, K), alkaline earth metals (Mg, Ca) or the addition of rare earth oxides (Ce, La, Pr) [3,8,24]. CeO_2 has been used as a support or promoter because its particular properties of oxygen storage and release that allow carbon deposits to be gasified and the presence of the Ce^{3+}/Ce^{4+} couple [25-27]. Other approach to enhance the properties of CeO_2 is doping ceria with other elements, such as Zr or Pr [28]. The incorporation of other cation with different size into the ceria structure to make oxygen release easier [26]. Elmhamdi et al. have also pointed out the importance of having CeO_2 at a nanometric level to enhance its properties [29]. In a previous work, the decrease of Ni and CeO_2 crystalline sizes on $Ni/MgAl_2O_4$-CeO_2 catalysts due to the use of chelating agents has been reported [30]. The system prepared in the presence of nitrilotriacetic acid (NTA), with a molar ratio of NTA/Ni=1 showed a good performance in ESR, obtaining high selectivity to H_2 and high resistance to carbon deposition [30]. In addition, the effect of EDTA/Ni molar ratio was examined in the synthesis of Ni catalysts [31]. The capacity of EDTA to form stable complexes with nickel and cerium promotes a better interaction between Ni and CeO_2 and decreases the size of NiO and CeO_2. A catalyst prepared using the stoichiometric ratio for the complete complexation of nickel (EDTA/Ni molar ratio=1) showed the best performance in ethanol steam reforming reaction under mild operation conditions and presented small crystallite size, and higher Ce^{3+}/Ce^{4+} and Ce/Ni^0 ratios.

In this work, the use of different amounts of NTA or CA as chelating agent in the synthesis of supported-Ni catalysts and their influence in ESR reaction are discussed.

2. Experimental

2.1. Catalyst Preparation

Nickel catalyst were synthetized following the procedure reported in [30]. Briefly, $MgAl_2O_4$ was prepared using citrate method and it was modified with CeO_2 (5 wt.%, nominal loading) by wet impregnation with an aqueous solution of $Ce(NO_3)_3.6H_2O$ (Aldrich, 99%). Nickel (8wt.%, nominal loading) was incorporated over the modified support, $MgAl_2O_4$-CeO_2 (in its dried form), using aqueous solution of $Ni(NO_3)_2 \cdot 6H_2O$ (Merck, 99%) in presence of chelating agent (L), NTA (Sigma-Aldrich, 99%) or CA (Sigma-Aldrich, 99.5%), in different L/Ni molar ratios (L/Ni = 0, 0.5, 1 and 2). First, the chelating agent was dissolved using a NH_3 solution and then $Ni(NO_3)_2 \cdot 6H_2O$ solution was added. The pH of these impregnation solutions was adjusted at a pH between 6-7 (lower than the PZC of $MgAl_2O_4$-CeO_2). The pH should be lower than the PZC to ensure a strong interaction between the complex with negative charge and the surface of support with a positive charge

[32,33].These solutions were aged under stirring at room temperature for 2 h. Then, 1 g of the $MgAl_2O_4$-CeO_2 was added and stirred for 1 h. The resulting suspensions were carried to an ultrasound bath at room temperature for 10 min and then the solvent was slowly removed under vacuum at 80 °C for 1 h. The dried samples were calcined in static air from room temperature to 650 °C at 10 °C min^{-1}. The catalysts were labeled as NiL(x), where x corresponds to the L/Ni molar ratio, being L= NTA or CA. NiL(0) corresponds to the nickel catalyst free of chelating agent.

2.2. Characterization of catalysts

Chemical composition. The solid samples were brought into solution by an alkali fusion with $KHSO_4$ and subsequent dissolution with aqueous HCl. Ni chemical composition was measured by atomic absorption spectroscopy using Varian AA 50 equipment. Cerium chemical composition was determined by inductively coupled plasma-atomic emission spectroscopy (ICP). A sequential ICP spectrometer Baird ICP 2070 (BEDFORD) with a Czerny Turner monochromator (1m optical path) was employed.

Adsorption-desorption N_2 isotherms. The specific surface area was determined by the BET method from the adsorption-desorption isotherms of N_2 at the boiling temperature of liquid nitrogen (-195.8 °C), using a Micromeritics Gemini 5 equipment. Previously, samples were degassed at 250 °C for 16 h in N_2 flow. From the desorption branch, pore size distribution values were obtained using the BJH model (Barreto, Joyner and Halenda) suitable for mesoporosity determination.

Temperature programmed reduction (TPR). The redox properties of the samples were examined using conventional equipment. Before to the TPR experiments, the samples were treated in O_2 flow (17%)/He (36 mL min^{-1}) at 300 °C for 1 h and then in He flow (30 mL min^{-1}) for 30 min. After cooling in He samples were reduced in flow of H_2(5 vol.%)/N_2 (50 mL min^{-1}) from room temperature up to 950 °C at 10 °C min^{-1}, keeping this temperature for 1 h.

Fourier Transformed Infrared spectroscopy (FTIR). The samples were analyzed by infrared spectroscopy using an FTIR Nicolet Protégé-460 spectrophotometer, in a range of 4000-250 cm^{-1} with a resolution of 4 cm^{-1} and 64 scans. The samples were mixed with KBr at approximately 1 wt.%, crushing the mixture into an agate mortar. Then, the mixture was compressed at a pressure of 300 Kg m^{-2} and room temperature.

UV-Vis and UV-Vis-NIR spectroscopy. The UV-Vis spectra of the different impregnation solutions were obtained using an Agilent 8454 spectrophotometer with diode network detector using the 8453 UV Visible ChemStation Rev.A.10.01 software, associated with the instrument. Catalytic samples were packed using $BaSO_4$ as blank and placed on the integrative sphere, ISR-3100. The Shimadzu UV-3600 was operated in diffuse reflectance mode in the UV-Vis–NIR (DR UV-Vis-NIR) range. The spectra for all samples were taken between 2500-200 cm^{-1} with a slit of 5 nm.

X-ray diffraction (XRD). The diffraction patterns of the samples were obtained in a RIGAKU (ULTIMA IV) diffractometer operated at 30 kV and 20 mA using CuKa radiation (λ=1.5418 Å) with Ni filter and horizontal goniometric. The data were acquired at 3° min^{-1}, for values of 2θ between 10 and 70°. The powder

samples were placed without any prior treatment in a flat glass sample holder. The identification of the crystalline phases was performed using reference patterns (JCPDS files of the ICDD). To study the crystallite size, the patterns were recorded in a step mode (2θ=10-90°; step = 0.02° and counting time: 5 s) and refined by the Rietveld method using the Fullprof program [34,35]. Figure S1 shows Rietveld refinements. For this purpose, the identified phases were considered with the following structural models: $MgAl_2O_4$ (cubic, $Fd\overline{3}m$), CeO_2 (cubic, $Fm\overline{3}m$), NiO (cubic, $Fm\overline{3}m$) and Ni (cubic, $Fm\overline{3}m$). The shape of the peaks was modeled using the Thompson-Cox-Hastings pseudo-Voigt function [36]. In some samples the crystallite size was obtained by applying the Scherrer equation [37]:

$$\beta = \frac{K\lambda}{d\,cos\theta}$$

β is the width of the peak that corresponds to a given value of 2θ, λ corresponds to the wavelength of the X-rays, K is a constant that is a function of the crystalline shape but it is generally taken equal to 0.9 for spherical particles and d corresponds to the crystallite size. The d value was manually obtained using the width of the following planes: (200) and (111) for NiO and CeO_2, respectively. The sizes of reduced samples were also obtained from Rietveld refinements where the size of each phase was automatically calculated by the program from all reflections and the Scherrer equation. In both cases the instrumental broadening was considered in the calculus.

X-ray photoelectron spectroscopy (XPS). XPS analysis was performed on a SPECS Multitechnical equipment equipped with an Mg/Al dual X-ray source and a PHOIBOS 150 hemiespheric analyzer in Fixed Analyzer Transmission (FAT) mode. The spectra were obtained with a pass-through energy of 30 eV and Al anode operated at 200 W. The pressure in the analysis chamber during the measurement was less than 2.10^{-8} mbar. To reduce the load effect on the samples, a "flood gun" electron cannon was used. Before acquisition of the spectra, samples were subjected to an in-situ reduction in H_2/Ar flow for 10 min at 400 °C, and then evacuated to a pressure less than 2.8×10^{-7} mbar for at least two hours before readings.

High resolution transmission electron microscopy (HRTEM). A TECNAI F20 FEI equipment with field emission source at 200 kV and a resolution of 0.19 nm was used for transmission electron microscopy. The samples were deposited in lacey-carbon Cu grids.

Thermal gravimetric analyses (TGA). The decomposition of the precursors of dried catalytic systems was performed in oxidizing atmosphere in a TGA 51 Shimadzu unit, with an air flow of 50 mL min^{-1} from room temperature up to 800 °C at 5 ° min^{-1}. The amount of carbon deposited on catalysts after the ESR reaction was studied in oxidizing atmosphere under an air flow of 50 mL min^{-1}, from room temperature to 900 °C with a heating rate of 10 °C min^{-1}. The samples were placed in a platinum capsule. The percentage of carbon deposited during the reaction for catalysts was calculated using the following equation:

$$\%C = \frac{(W_{initial} - W_{final}) * 100}{W_{final}}$$

($W_{initial}$ - W_{final}) is the amount of carbon on the catalyst and W_{final} is the final weight of the sample after TGA analysis.

Raman spectroscopy. Renishaw's inVia Qontor Raman microscope equipment was used. The spectra were taken with the visible laser of 532 nm with 15 accumulations (3 s), in the range between 600-1800 cm^{-1}.

Scanning electron microscopy and energy dispersive X-ray spectroscopy (SEM-EDAX). For qualitative determination of the local composition and texture of catalyst surfaces, a scanning electron microscope, LEO 1450 VP equipped with an EDAX Genesis 2000 microchannelizer with Si (Li) detector, was used. The samples were metalized with gold to prevent them from loading.

2.3. Catalytic experiments

Catalytic tests of the ESR reaction were carried out at 650 °C and atmospheric pressure, in a quartz tubular reactor (4 mm internal diameter), for 7 h. A previous *in-situ* reduction procedure was performed with a flow of H_2(5%) in N_2 for 45 min at 650 °C. The catalyst weight was 0.05 g with a particle size range between 0.3-0.4 mm (35-50 mesh) without dilution. The reactor feed consisted of liquid mixture of ethanol and water (0.15 mL min^{-1}), which was evaporated at 130 °C in a He flow free of O_2. The steam to carbon ratio, S/C, was equal to 2.5, with a composition of 9.4 % ethanol (y_{C2H5OH}) in the feed at an ethanol flow of 1.02 10^{-3} mol min^{-1}. The space-time was 0.018 g_{cat} h g_{C2H5OH}^{-1} (49 g_{cat} min mol_{C2H5OH}^{-1}). This reduced space-time allowed early detection of any deactivation effect [5].

Reagents and reaction products were analyzed on-line by two gas chromatographs. Catalytic activity experiments were performed in duplicate to verify their reproducibility and the percent of carbon deposition. The repeatability of data was in the range ± 5%. The catalytic experiments for NiNTA(0.5) and NiCA(1) were only run once. H_2, CH_4 and CO_2 were determined with TCD using N_2 as internal standard; while CO (previous passage through a methanator), C_2H_4O, C_2H_4 and C_2H_5OH without reacting and other compounds containing carbon, with the FID.

Ethanol conversion was calculated as:

$$X_{C2H5OH} = \frac{F_{C2H5OH}^{in} - F_{C2H5OH}^{out}}{F_{C2H5OH}^{in}} * 100$$

F_{C2H5OH} is the molar ethanol flow; *in* and *out* correspond to inlet and outlet flow of the reactor.

Selectivity to carbon products was calculated as:

$$S_i = \frac{ni\ F_i^{out}}{2\left(F_{C2H5OH}^{in} - F_{C2H5OH}^{out}\right)} * 100$$

F_i^{out} is the outlet flow of each hydrocarbon and *ni* is the number of carbon atoms in each product *i*.

Hydrogen yield was calculated as:

$$Y_{H2} = \frac{F_{H2}^{out}}{F_{C2H5OH}^{in}}$$

F_{H2}^{out} is the outlet flow of hydrogen of the reactor.

## 3. Results and discussion

3.1. Impregnation solutions

Thermodynamic speciation diagrams of nickel were obtained using Medusa Software [38]. They were calculated considering the ionic strength and the concentrations of each species present in the solution. Table 1 shows the predominant nickel species in impregnation solutions used in the synthesis of catalysts. The synthesis of catalysts was made by impregnation of support using a solution with a pH below to the PZC of the support (PZC=9.6 [30]) to ensure a strong interaction between the complex with negative charge and the surface of support with a positive charge. At pH of impregnation solution, the thermodynamic diagrams predict the formation of different nickel species at 25 °C. Only one complex species in solution, $[Ni(NTA)(H_2O)_2]^-$ and $[Ni(CA)_2]^{4-}$, was predicted by employing an L/Ni ratio leading to the most stable complex formation (NTA/Ni=1 and CA/Ni=2). Different nickel species in solution were predicted for the other L/Ni ratios and they could promote different interactions with the support affecting its catalytic properties.
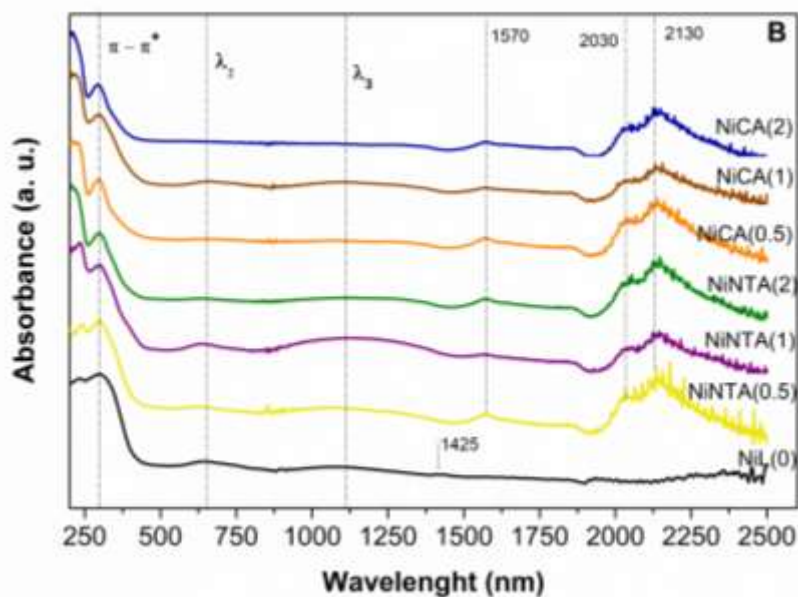
UV-vis spectra of the impregnation solutions allow to identify the nickel coordination in the solution, Figure 1A. The figure shows the UV-Vis spectra of the impregnation solution containing NTA and CA with different L/Ni molar ratio. In the UV zone it is observed at 300 nm the π-π* transition of the NO_3^-. The visible zone of the spectra shows the d-d transition of Ni^{2+} in an octahedral environment (Table S1 [39,40]), allowed transitions: λ_1: $^3A_{2g}$ (F) $\rightarrow$ $^3T_{1g}$ (P); λ_2: $^3A_{2g}$ (F) $\rightarrow$ $^3T_{1g}$ (F); λ_3: $^3A_{2g}$ (F) $\rightarrow$ $^3T_{2g}$ (F); and forbidden spin transition: λ_{fs}: $^3A_{2g}$ (F) $\rightarrow$ ^1E_g (D). The blue shift of the nickel bands using NTA or CA with different L/Ni ratios reveals the complex formation under the experimental synthesis conditions. The chelating agent, NTA or CA, produces a slight blue shift, indicating the complex formation by water substitution in $[Ni(H_2O)_6]^{2+}$ [41].

Table 1. Nickel species at pH of impregnation solutions.

System	pH	I*	Complex in solution
Solution L–Ni(0)	5.9	0.4	$[Ni(H_2O)_6]^{2+}$
Solution NTA–Ni(0.5)	6.6	1.3	$[Ni(NTA)(H_2O)_2]^-$; $[Ni(H_2O)_6]^{2+}$; $[Ni(NH_3)(H_2O)_5]^{2+}$
Solution NTA–Ni(1)	6.7	1.9	$[Ni(NTA)(H_2O)_2]^-$
Solution NTA–Ni(2)	6.6	2.3	$[Ni(NTA)(H_2O)_2]^-$; $[Ni(NTA)_2]^{4-}$
Solution CA–Ni(0.5)	6.5	1.6	$[Ni(CA)(H_2O)_2]^-$; $[Ni(CA)_2]^{4-}$; $[Ni(NH_3)(H_2O)_5]^{2+}$
Solution CA–Ni(1)	6.5	1.6	$[Ni(CA)_2]^{4-}$; $[Ni(CA)(H_2O)_2]^-$; $[Ni(NH_3)(H_2O)_5]^{2+}$
Solution CA–Ni(2)	6.6	2.4	$[Ni(CA)_2]^{4-}$

*I=Ionic strength. I was calculated as $I = \frac{1}{2}\sum_i c_i z_i^2$. c_i and z_i are the concentrations of each ion and its charge, respectively.
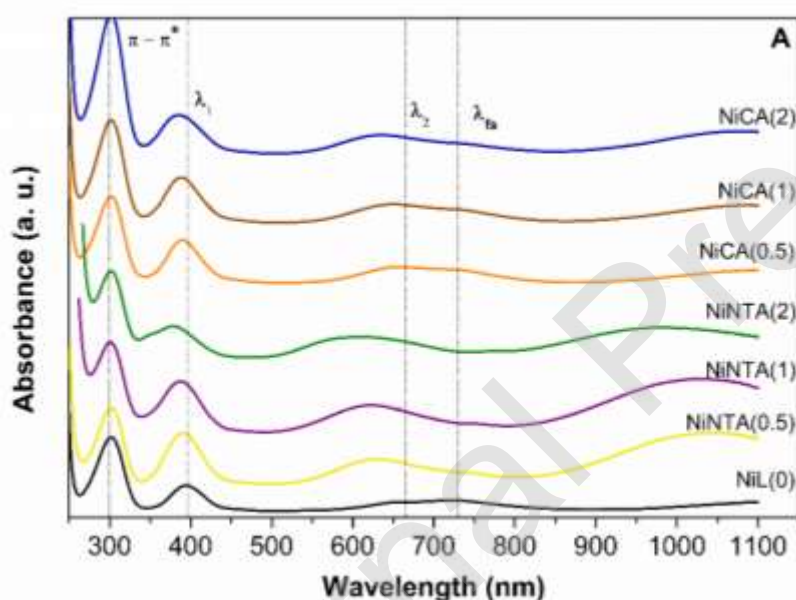
Figure 1. UV-Vis spectra of impregnation solutions (A) and DR UV-Vis-NIR spectra of dried catalysts (B).

3.2. Dried systems

The nickel coordination on the surface of dried catalysts was studied by DR UV-Vis-NIR spectroscopy. From a comparison between impregnation solution spectra and dried catalysts spectra it is possible to identify if the complex in solution is maintained in the dried system. Figure 1B shows the DR UV-Vis-NIR spectra of dried systems. Between 200-300 nm it is observed a band associated with $O^{2-} \rightarrow Ce^{4+}$ transition and/or $4f \rightarrow 5d$ of Ce^{3+} transition [42] or associated with charge transference between $O^{2-} \rightarrow Ni^{2+}$ [43]. In all spectra a band at 300 nm associated with the π-π* transition of NO_3^- without coordination is observed, interacting only by physical adsorption with the support [42,44]. Table S1 shows the transitions in dried systems compared to impregnation solutions. For all dried systems, in the Vis-NIR zone, two bands are observed, λ_2 and λ_3, between 500 and 1500 nm, while the λ_1 transition could be overlapped with the band at 300 nm. In the NiL(0) dried sample a slight blue shift is noticed respect to the bands in its impregnation solution. This indicates that the nickel aquocomplex, $[Ni(H_2O)_6]^{2+}$, is interacting as such with the support. The positions of the bands in the NiNTA(x>0) dried samples have experimented a slight red shift respect to bands of impregnation solutions. The same occurs in the NiCA(0.5) and NiCA(1) dried samples. Unexpectedly, the Ni^{2+} bands are of low intensity in the NiCA(2) system. The red shift or towards higher wavelength values indicate that the nickel complex on the surface is a lower strength field. This red shift is related to a bonding weakening among the chelating and Ni^{2+} by formation of hydrogen bonding between OH groups of the support and the oxygen atoms of the chelating agent. During drying step the chelated metal precursor forms a gel-like phase and this gel would sufficiently interact with the support [9]. Ortega-Domínguez et al. [45] have informed similar

results using a Ni-EDTA impregnation solution over SBA-15. Koizumi et al. [46] have also reported the same interaction between NTA and Co^{2+} in the solution and claimed that it was maintained on the dried surface of Co catalysts synthesized with NTA. NIR zone, between 800-2500 nm, shows a band around 1570 nm corresponding to the first overtone of $\nu(NH)$ vibration [47]. Between 1500 and 2500 nm vibrations related to chelating structures are observed (they are not present in the NiL(0) dried spectrum). NiL(0) dried sample only shows a band at 1425 nm that corresponds to the first overtone of OH neutral species. In the NiNTA(x>0) or NiCA(x>0) major differences with the increase of chelating agent are not observed, indicating that the nickel complex on the surface of the dried systems could have the same nature.

In order to identify the species on the surface in the dried systems, samples were examined by FT-IR analyses (Figure 2). All the systems prepared with NTA or CA show, between 2600 and 3700 cm^{-1}, a band associated with OH group vibrations (3470 cm^{-1}) and bands related to symmetric and asymmetric stretching of CH_2 (3140-2800 cm^{-1}) [48]. In 1630 cm^{-1} the band of H_2O deformation (δH_2O) appears [49]. The characteristic sharp bands of nitrate are observed in agreement with the NO_3^- π-π^* transition assigned in UV-Vis spectroscopy. In particular, the transitions of nitrate ion at 826 and 1765 cm^{-1} are observed in all the dried samples and the transitions at 1393 and 1630 cm^{-1} are less notorious in the systems prepared with chelating agents. The bands detected between 1700-1200 cm^{-1} correspond to the contribution of carboxylates group bonded to a metal and the presence of nitrate ion without coordination [50]. Furthermore, it is not observed an additional band to values higher than 1630 cm^{-1} indicating the absence of carboxylates without coordination [51,52]. The major contribution for all the dried systems prepared with NTA or CA correspond to the symmetric stretching of COO^- (ν_s) and asymmetric stretching of COO^- (ν_{as}) [53] and it indicates that the metal is coordinated by carboxylate groups belonging to chelating agents regardless of the L/Ni molar ratio used.
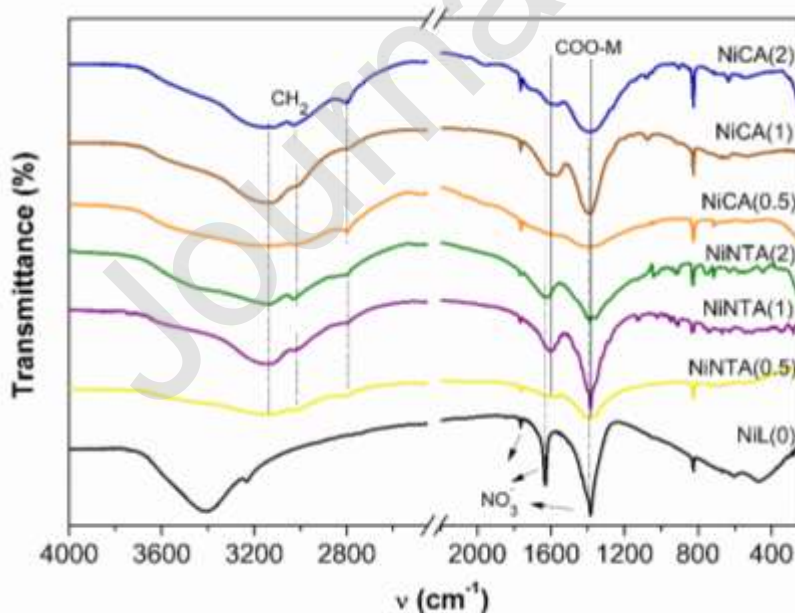
Figure 2. Infrared spectra of dried catalysts.

Infrared spectra of fresh systems (Figure S2) show symmetric and asymmetric bands of COO⁻ groups. This carbonaceous species corresponds to wastes of the synthesis of the support. They remain after the combustion of citric acid used in $MgAl_2O_4$ preparation at 650 °C for 3 h [31]. It is not observed differences in the spectra of calcined samples when NTA or CA is used in the impregnation solutions. This indicates that the vibrational nature of oxide species is similar in all catalysts independently of chelating agent and the quantity used.

Thermal decomposition of precursor was studied under an oxidant atmosphere. Figure S3 shows the thermograms and dweight/dt vs. temperature of dried catalysts where different weight loss events are observed. The theoretical weight losses considering that precursor decomposition leads to NiO are shown in Table S2. The experimental values are lower than the theoretical ones, except for the NiCA(0.5) sample. Similar results were observed with catalysts prepared with EDTA [31], suggesting that the decomposition began in the dried step. In the sample free of chelating agent, NiL(0), the weight loss up to 100 °C could be assigned to the elimination of physisorbed water, and that at 300 °C corresponds to the combustion of the precursor to produce NiO [54]. For the NiNTA(x>0) systems differences are observed in the number of weight loss events associated to decomposition of different precursor species. NiNTA(0.5) shows significant weight loss from 230 °C to constant weight at 400 °C. The maximum decomposition temperature at 245 °C is associated to the decomposition of the nickel aquocomplex and the complex with NTA. The maximum decomposition temperatures are detected at 231, 294 and 360 °C for NiNTA(1), while two weight loss events are observed at 245 °C and around 375 °C for NiNTA(2). The latter event is related to decomposition of free NTA. In the NiNTA(x>0) systems are not possible to dismiss the Ce-NTA complex formation. NiCA(0.5) only shows a weight loss at 245 °C, while in NiCA(1) are observed three weight loss events at 233, 278 and 358 °C. The main weight loss is shown at 243 °C and the smallest one at 393 °C for NiCA(2). The presence of a weak peak between 300 and 500 °C is only observed in NiCA(1) sample. Probably the interaction between CA and Ce is negligible, its stability constant is lower in comparison with NTA. Wang et al. [48] have studied the decomposition in air of $Na_2[Ni(CA)]$. These authors have identified two combustion events: a weight loss between 30-340 °C attributed to coordinated water removal and CO_2 release, and the latter in the range of 340-520 °C to the combustion of the organic component. They did not observe mass changes at temperatures below 300 °C, and it is considered that some of the H_2O were incorporated into the structure of the complex like $[Ni(CA)(H_2O)_3]$.

3.3. Fresh and reduced catalysts

Table 2 shows the values of chemical composition obtained for the catalysts. Nickel and cerium content were lower than the nominal values probably due to the precursor salts that are easy to hydrate. For NiNTA(2) and NiCA(2) the Ni values are higher and this fact will contribute to its catalytic performance. N_2 adsorption-desorption isotherms are shown in Figure S4A. The isotherms are IV type with H2 hysteresis for all the catalysts in this work, this is typical of mesoporous solids with cylindric porous or aggregates or

agglomerates of spherical particles with non-uniform size and shape [55]. The S_{BET} values are presented in Table 2. A decrease in all the catalysts respect to the support, $MgAl_2O_4$-CeO_2, $S_{BET} = 102$ g m^{-2} is observed. This decrease could be related with the thermal treatment after the impregnation step or the porous blockage by NiO phase impregnated [56]. The S_{BET} for the catalysts is not affected by the nature of the chelating agent or for the L/Ni molar ratio. Pore size distribution (Figure S4B) is similar for all the catalysts independently of the precursor used in the synthesis. The catalysts have larger porous respect to $MgAl_2O_4$-CeO_2, with a high contribution of porous between 2 and 8 nm and an increase in the porous size associated with decomposition of precursor during the calcination step [57].

**Table 2**. Some properties of catalysts synthesized with NTA and CA.

Sample	Ni wt.%	CeO$_2$ wt.%	S_{BET} (m^2 g^{-1})	d_{pore} (nm)	V_{pore} (mL g^{-1})
NiL(0)	5.7	4.4	88	4.9	0.14
NiNTA(0.5)	6.5	4.7	95	4.7	0.14
NiNTA(1)	6.3	5.4	92	5.8	0.17
NiNTA(2)	8.2	5.6	99	5.0	0.15
NiCA(0.5)	6.8	5.2	91	5.0	0.13
NiCA(1)	5.0	4.5	80	5.4	0.14
NiCA(2)	9.0	4.5	94	4.9	0.15
MgAl$_2$O$_4$-CeO$_2$	--	n.d.	102	4.4	0.08

n.d.= not determined

X-ray patterns of fresh catalysts are shown in Figure S5. $MgAl_2O_4$, CeO_2 and NiO phases are observed in all the catalysts. Table 3 shows the crystallite size of NiO and CeO_2 phases determined by Scherrer equation (between brackets) using the peaks in $2\theta = 43°$ and $28°$, respectively. The broadening of the peaks in $2\theta = 43°$ of the NiO phase shows that the use of NTA promotes the formation of smaller NiO crystallites regardless of the amount of used NTA respect to the NiL(0). In addition, NiNTA(1) and NiNTA(2) samples show a broadening of peak in $2\theta = 28°$ corresponding to CeO_2, this effect is less notorious in the NiNTA(0.5) system. $MgAl_2O_4$-CeO_2 support is used without calcination, and it has been verified that a CeO_2 dissolution occurs during impregnation step [31]. Similar results were reported by Santolalla-Vargas et al. [58] in the preparation of W catalysts. The authors have noted a redispersion of W on the surface when the impregnation solution containing CyDTA as a chelating agent is mixed with dried γ-Al_2O_3 support promoting the formation of different W species. 0.5 NTA mol per Ni mol would promote the complexation only of Ni^{2+} ion while a higher amount of NTA (NTA:Ni = 1 or 2) could also afford an interaction with Ce^{3+} in the solution. The redispersion of ceria on the NiNTA(1) and NiNTA(2) samples allows its redeposition as amorphous particles or smaller crystallites. CeO_2 crystallite size reduction induces changes in its properties allowing an effective interaction with nickel phases on the surface. Moreover, this interaction between Ni and Ce promoted by the use of chelating agent has started in the impregnation solution [30,59]. The use of the CA also promotes the NiO

crystallite size decrease and a slight effect in those of CeO_2, Table 3. This allows to infer that the CA rather interacts with Ni^{2+} and not with Ce^{3+}, in agreement with that observed by TG analysis (Figure S3).

X-ray diffractograms of reduced catalysts are shown in Figure 3. $MgAl_2O_4$, CeO_2, Ni and NiO phases are identified in all diffraction patterns. The crystallite sizes of the phases are shown in Table 3.
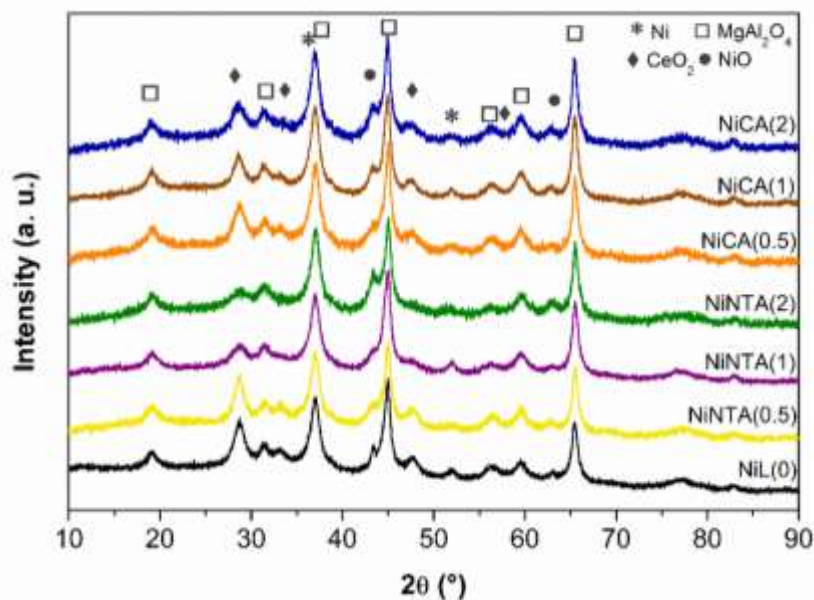
Figure 3. XRD patterns of reduced catalysts.

Table 3. Crystallite size of reduced catalysts from Rietveld refinement.

Sample	d_{Ni}^{XRD} (nm)	d_{NiO}^{XRD} (nm)*	$d_{CeO_2}^{XRD}$ (nm)*	$d_{MgAl_2O_4}^{XRD}$ (nm)
NiL(0)	4.0	13.0 (13.1)	6.0 (4.6)	5.3
NiNTA(0.5)	2.2	5.9 (7.1)	6.1 (8.9)	5.2
NiNTA(1)	4.0	6.6 (9.3)	2.7 (~ 4)	5.0
NiNTA(2)	2.0	6.6 (9.5)	1.9 (5.5)	5.0
NiCA(0.5)	2.6	4.3 (8.8)	4.4 (6.0)	4.9
NiCA(1)	3.3	7.4 (12.4)	4.4 (6.3)	4.9
NiCA(2)	2.1	6.5 (9.3)	3.2 (7.5)	4.9

* Values between brackets correspond to crystallite size of fresh

catalysts obtained with Scherrer equation.

The presence of NiO phase reveals that reduction during 45 min at 650 °C under H_2/N_2 flow was incomplete. The intensity of this peak in $2\theta = 43°$ is high in the NiL(0), NiNTA(2) and NiCA(1) samples related to the presence of major amount of Ni^{2+} species that are hard to be reduced. Between 50 and 53° a Ni^0 peak is observed. Ni^0 crystallite size of catalysts prepared with NTA follows the order: NiNTA(2) ~ NiNTA(0.5) < NiL(0) ~ NiNTA(1). The CeO_2 crystallite size follows the order: NiNTA(2) ~ NiNTA(1) < NiL(0) ~

NiNTA(0.5). The use of the molar ratio NTA/Ni=2 generates smaller Ni^0 and CeO_2 crystallites. XRD of NiNTA(2) also shows a high intensity of NiO peak, probably by an excess of nickel content in this sample. The use of CA leads to smaller Ni^0 crystallite size respect to NiL(0), Table 3. In NiCA(x) systems, the Ni^0 crystallite size follows the order: NiCA(2) < NiCA(0.5) < NiCA(1) < NiL(0). The CeO_2 crystallite size follows the order: NiCA(2) < NiCA(0.5) ~ NiCA(1) < NiL(0). Li et al. [60] have reported a decrease in the size of NiO crystallite and Ni^0 in reduced Ni/SiO_2 catalysts calcinated at 500 °C and prepared in the presence of citric acid. These authors have reported that the smallest crystallite size was obtained using a molar CA/Ni ratio of 1.5.

The DR UV-Vis-NIR spectra of fresh catalysts, Figure S6, shows that the phase NiO is the predominant one on the catalysts and that it has not been influenced by the chelating agent or the employed amount in the synthesis. This behaviour is related to the stability of the support not allowing the nickel spinel formation. The most intense band at 263 nm would be associated to a process of charge transference between $O^{2-} \rightarrow Ni^{2+}$ [43]. Bands around 720 and 1190 nm would correspond to Ni^{2+} transitions with an octahedral environment. The bands at 583 and 624 nm associated to the presence of $NiAl_2O_4$ phase were not detected [61,62]. This indicates that all the catalytic systems exhibit Ni^{2+} species with a similar coordination environment regardless the addition of NTA or CA.

From TPR profiles it is possible to identify the influence of amount of chelating agent used in the synthesis on the reducibility of different species, Figure 4. All the TPR profiles are broader indicating the presence of different species. From a comparison with some results reported in literature on reducing systems containing Ni, Ce, Mg and/or Al, Table 4, the peaks in the TPR profiles could be assigned to the following species:

α species (between 200-400 °C): CeO_2 surface reduction and/or NiO amorphous species reduction;

β species (between 400-600 °C): reduction of Ni^{2+} species interacting with CeO_2 and/or Ni^{2+} species slightly interacting with $MgAl_2O_4$;

γ species (between 600-800°C): reduction of Ni^{2+} with a high interaction with $MgAl_2O_4$;

*δ species*: reduction of CeO_2 bulk above 750 °C.

The *γ species* were only assigned to Ni^{+2}-$MgAl_2O_4$ interactions due to the absence of DR UV-Vis-NIR bands associated to $NiAl_2O_4$, Figure S6.

The reduction profile of NiNTA(2) is similar to NiL(0), although the γ species reduce to higher temperatures. The same is observed in NiNTA(0.5) sample. The sharp peak on the TPR profiles of systems prepared with NTA is associated with β species indicating that this chelating agent promotes an intimate contact between Ni^{2+} and CeO_2. NiNTA(1) profile suggests a major contribution of β species in comparison with the other NTA-systems. This redox behaviour was verified by performing a complementary TPR experiment up to a final temperature of 700 °C on an automatic Micromeritics AutoChem II equipment. The profile showed the same behaviour, Figure S7.

Table 4. Reduction of Ni^{2+} and/or Ce^{4+} species in the literature.

Catalytic system	TPR conditions	Reduction events	Ref.
Hydrotalcites Ni-Mg-Al-Ce	10 °C min^{-1} 80 mL min^{-1} H$_2$(5 %)/N$_2$	The incorporation of: –Ce produces a reduction of nickel spinel at lower temperatures. –Ni^{2+} into the CeO$_2$ network forms a solid solution allowing reduction to lower temperatures that overlap with the less interacted Ni^{2+} reduction peaks.	[49]
Ni(10wt.%)-Ce (2.5wt.%)/MgAl$_2$O$_4$	10 °C min^{-1} H$_2$(10 %)/Ar	The reduction starts in the Ni-Ce/MgAl$_2$O$_4$ system at 200 °C. The surface reduction appears at temperatures above 350 °C with the increase of Ce. The peak at: –550 °C is attributed to Ni^{2+} species in interaction with CeO$_2$ –780 °C is attributed to reduction of complex NiO species that interact strongly with MgAl$_2$O$_4$.	[59]
Ni(7wt.%)/CeO$_2$-MgO	10 °C min^{-1} 50 mL min^{-1} H$_2$(5 %)/Ar	The peak at: –450 °C is attributed to superficial reduction of CeO$_2$. –315 °C is attributed to reduction of bulk NiO.	[63]
Ni/MgO (2.5, 6.25, y 12.5wt.%)-Al$_2$O$_3$ Ni from Ni(II)-ethylenediamine (en/Ni=2)	10 °C min^{-1} 40 mL min^{-1} H$_2$(5 %)/Ar	α species assigned to the reduction of bulk NiO or free NiO without direct interaction with support or species with a very weak interaction. β1 species are NiO species in a Ni-riched mixed with greater interaction than α species. β2 species attributed to NiO in a Al-riched mixed phase. γ species assigned to the Ni spinel strongly associated with the spinel structure.	[64]
Ni(1.5, 4.5, y 10wt.%)/MgAl$_2$O$_4$	10 °C min^{-1} 40 mL min^{-1} H$_2$(10 %)/N$_2$	The broad peak between 300 and 400 °C is attributed to reduction of NiO. The small shoulder at high temperatures corresponds to the reduction of the aluminate phase of Ni The peak at low temperatures of large NiO particles without interaction with the support.	[65]
Hydrotalcites Ni(>9wt.%)/Mg/Al	10 °C min^{-1} 30 mL min^{-1} H$_2$(5 %)/N$_2$	The peak around 800 °C is attributed to the reduction of NiO with strong interaction with MgO and/or Al$_2$O$_3$.	[66]
Ni/xMg-ATP x=0, 5, 10, 20 wt.% ATP: attapulgite	10 °C min^{-1} 40 mL min^{-1} H$_2$(10 %)/Ar	Peaks between: –300-500 °C attributed to NiO with a slight interaction with γ-Al$_2$O$_3$. –500 and 700 °C attributed to a solid nickel-aluminate solution. –700 and 900 °C attributed to NiO species with strong interaction with γ-Al$_2$O$_3$.	[67]
Ni(8wt.%)/ MgAl$_2$O$_4$	30 mL min^{-1} H$_2$(10 %)/N$_2$	The broad peak at 265 °C is attributed to the reduction of NiO that interacts weakly with the spinel. The peak at 710 °C to small NiO particles with strong interaction with the support.	[68]
Mixed oxides CeNi$_x$O$_Y$	10 °C min^{-1} 33 mL min^{-1} H$_2$(5 %)/Ar	The low temperature peak is attributed to a solid solution between Ni and Ce or small NiO particles.	[69]
Ni(>9.1wt.%)/γ-Al$_2$O$_3$	10 °C min^{-1} 40 mL min^{-1} H$_2$(5%)/Ar	Peaks between: –350-500 °C attributed to amorphous NiO. –500-520 °C attributed to crystal NiO. –520-700 °C attributed to NiAl$_x$O$_y$ (a deficient-Ni-state compound). –650-800 °C attributed to NiAl$_2$O$_4$.	[70]
Ni(2wt.%)@SiO$_2$@CeO$_2$ (27.6%wt.%)	5 °C min^{-1} 30 mL min^{-1} H$_2$(3.2%)/N$_2$	The peak at: –351 °C associated with surface lattice oxygen removal in CeO$_2$. –447 °C associated to reductions of Ni species that have weak Ni-SiO$_2$ interaction. –730 °C related to reduction of Ni species that have strong Ni-SiO$_2$ interaction.	[71]

Also, NiCA(0.5) and NiCA(1) have a notorious presence of species with intermediate reduction temperatures between 400 and 600 °C. TPR profile of NiCA(2) is similar to NiL(0), but it is evidenced a major contribution of β species. The use of NTA or CA produces the reduction of γ species at higher temperature and promotes a major contribution of β species that reduce at a lower temperature respect to NiL(0) regardless the amount of chelating agent used.
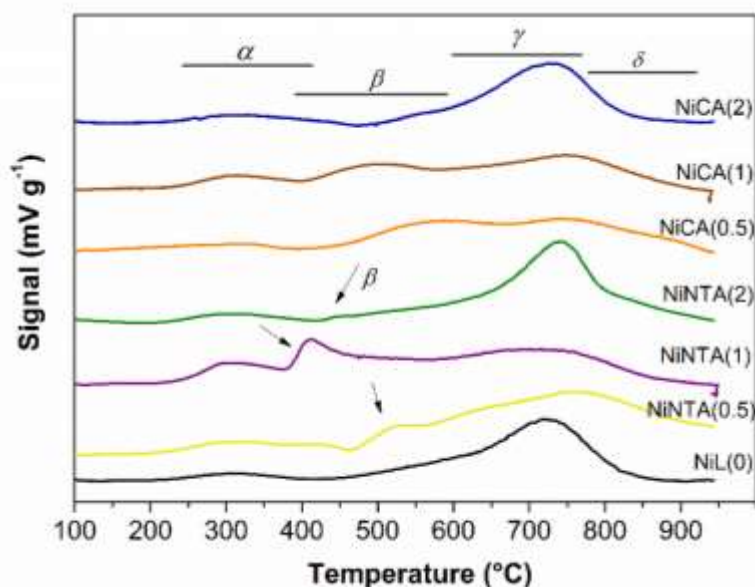
Figure 4. TPR profiles of fresh catalysts.

The influence of the amount of NTA or CA on redox properties is also studied by X-ray photoelectron spectroscopy. XPS spectra are shown in Figure 5. Fresh catalysts were reduced *ex situ* at 650 °C for 45 min in $H_2(5\%)/N_2$ flow. Before recording XPS spectra, the samples were *in situ* reduced at 400 °C for 10 min in the pre-chamber of the equipment, so that the contribution by Ni^0 oxidation in contact with the atmosphere can be considered negligible. The presence of Ni^{2+} in the reduced samples is related to the used reduction conditions, in agreement with what was observed in the XRD patterns, Figure 3. Binding energy (BE) values of the different peaks belonging to Ce 3d and Ni 2p are presented in Table S3. The BE values of Ni^{2+} and Ni^0 can be assigned near to 855 and 852 eV, respectively. A slight decrease in BE values of Ni 2p is observed with the use of NTA and CA, Table S3. This decrease is an indication that the addition of chelating agents increases the electronic density of Ni species. A "memory effect" of Ni species seems to be present generating different environments in the catalysts prepared from chelating agents [44]. It has been reported that the decrease in BE of Ni $2p_{3/2}$ is related to higher interaction between Ni and CeO_2 [62,72], which it has been also identified with the increase in the atomic ratio Ce/Ni^0 for catalysts prepared with chelating agents. In the Ce 3d region, peaks belonging to Ce^{4+} and Ce^{3+} are also observed. The presence of the Ce^{3+}/Ce^{4+} redox couple participates in carbon removal reactions and its presence increases tolerance to carbon deposition, Table 5. The values of the Ce^{3+}/Ce^{4+} ratio are higher in the NiNTA(1) and NiNTA(2) systems, being equal to 1.5, while for the sample prepared without chelating agent or with 0.5 mol of NTA, the Ce^{3+}/Ce^{4+} ratio is 0.7. This increase in the

degree of surface reduction of ceria is associated with an improvement in the oxygen mobility [73], due to the nanometric size of the ceria and its better interaction with nickel. The higher Ce^{3+}/Ce^{4+} ratio values correspond to systems with smaller crystallite sizes of CeO_2, NiNTA(1) and NiNTA(2), Table 3. For the NiCA(1) sample, the Ce^{3+}/Ce^{4+} ratio is 1.0. As it was already mentioned, the presence of the Ce^{3+}/Ce^{4+} redox couple participates in carbon removal reactions and its presence is key for increasing carbon deposition tolerance.
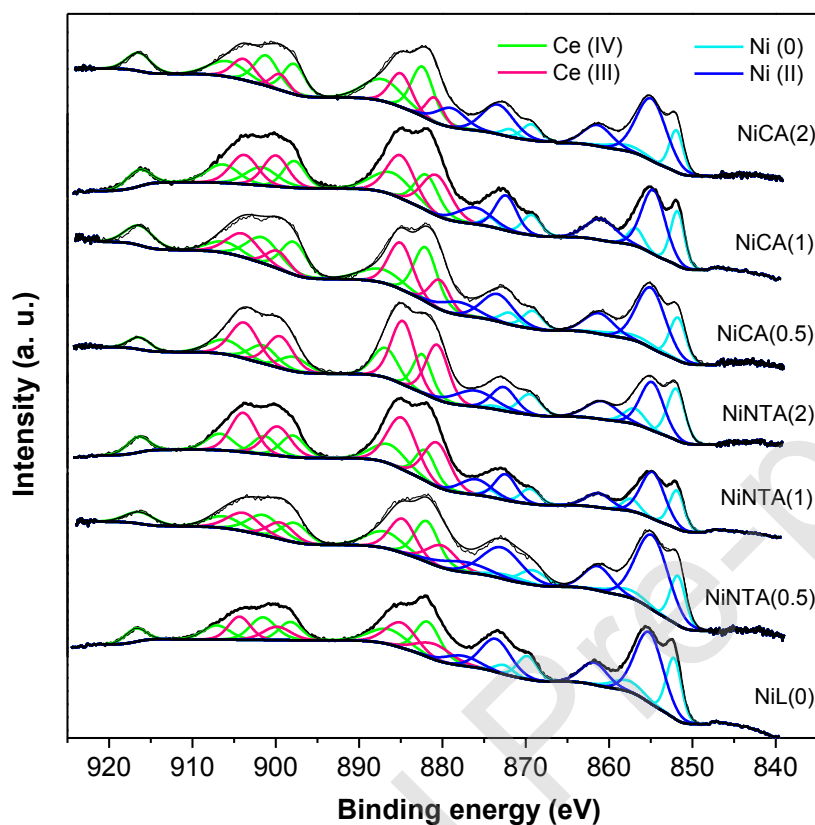
Figure 5. XPS spectra of reduced catalysts.

**Table 5.** Surface atomic ratio from XPS of reduced catalysts.

Sample	Ce^{3+}/Ce^{4+}	Ni^0/Ni^{2+}	Ce/Ni^0	Ni^0/Ni	Ni/Σ^*	Ce/Σ^*
NiL(0)	0.7	0.5	1.26	0.33	0.09	0.04
NiNTA(0.5)	0.7	0.3	1.70	0.25	0.12	0.05
NiNTA(1)	1.5	0.5	2.80	0.34	0.07	0.06
NiNTA(2)	1.5	0.4	1.82	0.42	0.13	0.09
NiCA(0.5)	0.6	0.4	2.21	0.29	0.09	0.06
NiCA(1)	1.0	0.5	2.27	0.32	0.06	0.04
NiCA(2)	0.4	0.3	2.30	0.24	0.11	0.06

* Σ= Ni+Ce+Al+Mg

The Ni^0/Ni surface ratio, considered as a measure of Ni^0 dispersion, increases with the increase of NTA in NiNTA(x) systems, Table 5. However, it does not show a clear dependence with the amount of CA. The obtained values for NiCA(x) are very similar to each other, in agreement with the smaller differences in crystallite sizes determined by XRD. It can be inferred that the addition of CA in the preparation produces slight changes in Ni^0 dispersion. The Ce/Ni^0 surface ratio, considered as a measure of the $Ni-CeO_2$ interaction, changes with the NTA/Ni molar ratio and follows the order of NiL(0) (1.26) < NiNTA(0.5) (1.70) < NiNTA(2) (1.82) < NiNTA(1) (2.80). The highest value is obtained for the NiNTA(1), catalyst that presented a TPR sharp peak related to the reduction of Ni^{2+} species interacting with CeO_2 (β species). In the same way, the Ce/Ni^0 surface ratio clearly increases by using CA in preparation, following the order of NiL(0) (1.26) < NiCA(0.5) (2.21) < NiCA(1) (2.27) < NiCA(2) (2.30).

Representative HRTEM images of NiL(0), NiNTA(1) and NiCA(2) samples are shown in Figure 6. From these images it is possible to identify different phases. These systems revealed the presence of Ni^0, NiO, CeO_2 and $MgAl_2O_4$ crystalline phases. The Fourier Transform images in different zones of the reduced catalysts show spots at 0.25-0.26 nm and 0.21 nm corresponding to (1 1 1) and to (2 0 0) crystallographic planes of NiO, respectively; spots at 0.25-0.26 nm and 0.20-0.21 nm corresponding to (3 1 1) and to (4 0 0) planes of $MgAl_2O_4$; spots at 0.26 nm and 0.30-0.33 nm corresponding to (2 0 0) and (1 1 1) planes of CeO_2 and spots at 0.19-0.21 nm of (1 1 1) plane of Ni^0. In the images CeO_2 particles with sizes less than 10 nm are observed in concordance with the crystallite size obtained from XRD, Table 3.
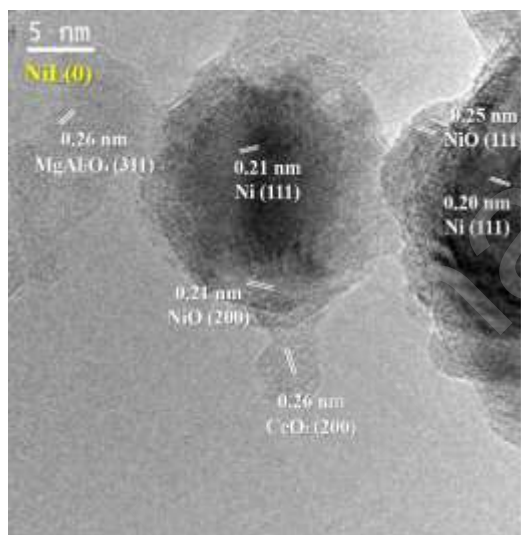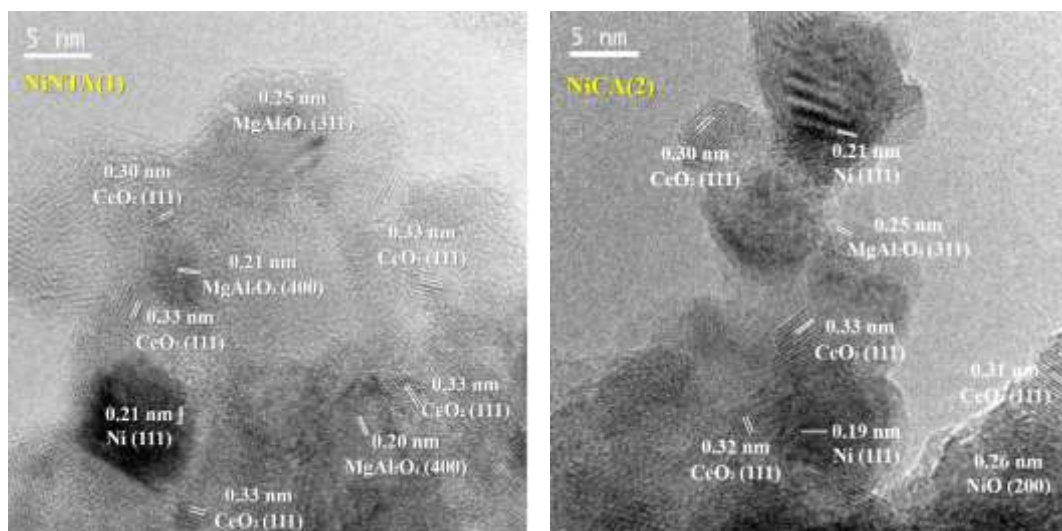
**Figure 6.** HRTEM images of reduced catalysts.

3.4. Ethanol steam reforming

All catalysts were tested in ethanol steam reforming reaction, Figure 7. Under the operation conditions (without bed dilution and $y_{C2H5OH} = 9.2$ %) used in this study, an early deactivation on the catalysts could be observed. As already mentioned, all catalysts were *in situ* reduced before an experimental run. For catalysts prepared with NTA, the ethanol conversions were higher than 80 %. In particular, the NiL(0) and NiNTA(1) catalysts were the most active, presenting average conversions of 98 and 97 %, respectively, with a slight loss of activity with operating time. The NiNTA(0.5) and NiNTA(2) samples were less active with average conversions of 86 and 91 % and a loss of activity of about 11% after 7 hours in operation. The main products were H_2, CO and CO_2 and less amount of CH_4, C_2H_4O and C_2H_4. Selectivity to H_2 exceeded 70 %. Its average yield, expressed as H_2 mol per ethanol-fed mol, follows the order: NiNTA(0.5) (4.3) < NiNTA(2) (4.6) < NiL(0) (5) < NiNTA(1) (5.3 mol H_2 mol $C_2H_5OH^{-1}$). The NiL(0) system had the lowest selectivity to CO_2, around 43 %, while those systems prepared with NTA reached values of 50 %. CO selectivity was higher for the chelating-free system, being lower for NiNTA(0.5) and NiNTA(2) systems. For NiNTA(0) and NiNTA(1), the selectivity to minority products: CH_4, C_2H_4O and C_2H_4, were below 6 %; while in NiNTA(0.5) and NiNTA(2), the formation of these products was higher with significant selectivities to CH_4 and to C_2H_4O. In all systems, selectivity to C_2H_4 was lower than 1.5 %. The higher selectivity of methane, of course, affects selectivity to H_2 [74]. CH_4 can be formed by the decomposition of ethanol ($C_2H_5OH \rightarrow CH_4 + CO + H_2$), and/or by the methanation of CO and CO_2 [75,76]. The catalytic results of the NiNTA(2) system are unexpected, taking into account the small size of the Ni^0 and CeO_2 and the high Ce^{3+}/Ce^{4+} ratio. The presence of a higher amount of Ni in its oxidized form, at the beginning of the reaction and after reduction (XRD of the reduced system, Figure 3), possibly affects the different stages in the reaction mechanism, promoting secondary reactions of formation of CH_4, C_2H_4O and C_2H_4. The best catalytic behaviour was observed for the

NiNTA(1) catalyst, which corresponds to the stoichiometric ratio of the most stable complex between nickel and nitrilotriacetic acid. Although, in NiNTA(1) was evidenced a slight deactivation that could be related to the type of carbon on the surface.

For all catalysts prepared with CA, the ethanol conversions were higher than 90 %. The distribution of the products showed slight variations. The major products were H_2, CO_2 and CO, being the selectivity to H_2 higher than 80 % in all the cases. The NiCA(2) system exhibited a complete ethanol conversion during 7 h, while the other three CA-systems showed a slight decrease in activity. Its H_2 average yield follows the order: NiL(0) (5.0) < NiCA(0.5) (5.2) < NiCA(1) (5.5) < NiCA(2) (5.6 mol H_2 mol $C_2H_5OH^{-1}$). The most important differences were on the quantity of secondary products, such as CH_4, C_2H_4O and C_2H_4. The use of CA leads to a sightly increase in the amount of CH_4. C_2H_4O and C_2H_4 were also observed in small quantities on NiCA(0.5) and NiCA(1). For NiCA(1) a slight decay in CH_4 production with an increase in C_2H_4O was detected with time on stream, perhaps by a loss of activity in the C_2H_4O decomposition reaction [8]. From the analysis of these results, the NiCA(2) catalyst showed the best catalytic behaviour. This sample presented the smallest Ni^0 crystallite size and a high Ce/Ni^0 ratio. Besides, the CA:Ni molar ratio corresponded to the stoichiometric ratio to form the most stable complex between nickel and citric acid.

A direct comparison of catalytic behaviour between Ni catalysts tested in ESR is difficult due to not only catalyst features (metal percentage, support, modifiers, etc.) and synthesis conditions (different precursor salts and preparation methods) but also to significant changes in the reforming conditions (steam to carbon ratio, temperature, catalyst weight, degree of bed dilution, percentage of ethanol in the feed and activation conditions). Bepari et al. [49] have studied a series of cerium-promoted Ni-Mg-Al hydrotalcite catalysts in the ESR. The best performance was obtained at 540 °C (operation conditions: 3.0 g_{cat}, S/C ratio = 4.5 and space-time of 22.04 kg_{cat}h kmol^{-1} of ethanol fed) for the 5.5 % Ni and 10.5% Ce catalyst. Under this condition, about 97 % of ethanol conversion was obtained with a H_2 yield of 4.3 mol H_2.mol $C_2H_5OH^{-1}$, also were detected CO_2, CO and CH_4 as products. Słowik et al. [19] prepared a Ni/CeO_2 catalyst using an aqueous solution of nickel nitrate with citric acid CA (Ni/CA =1), calcined at 420 °C and reduced with hydrogen at 420 °C for 1 h. This catalyst was 100 % active in the ESR (operation conditions: 0.1 g_{cat} with dilution and S/C ratio = 6) at 420 °C for 30 h, the main products were H_2 (68 to 75%), CO_2 (58 to 60%) and CH_4 (41 to 35%) with traces of CO and C_2H_4O.
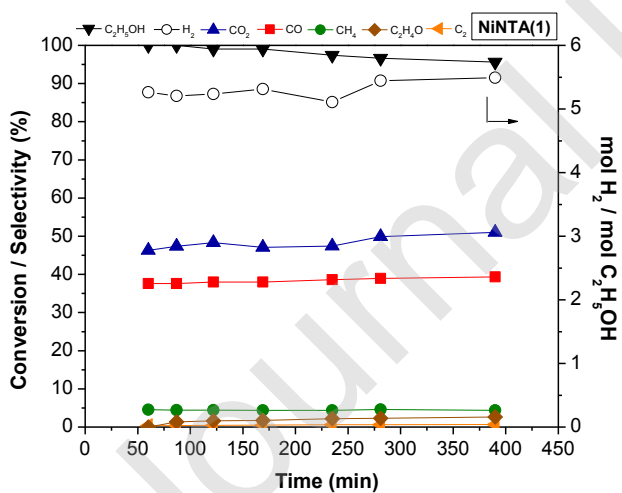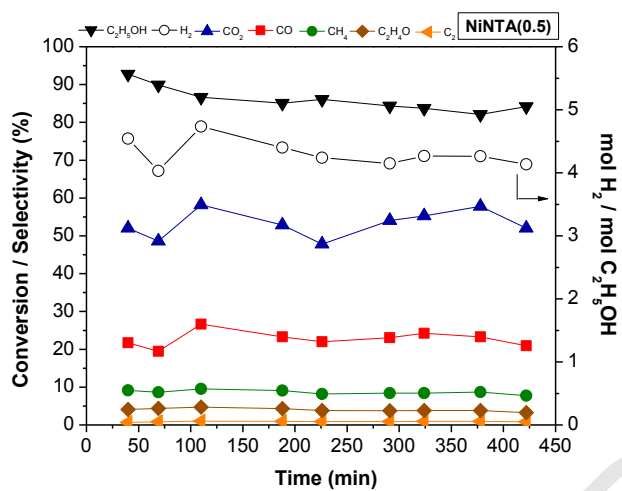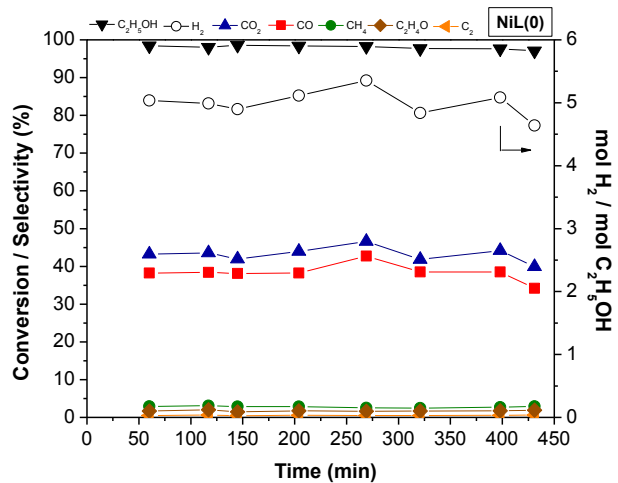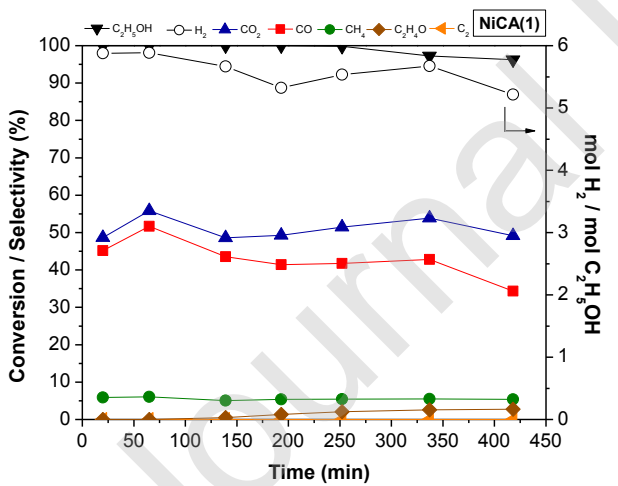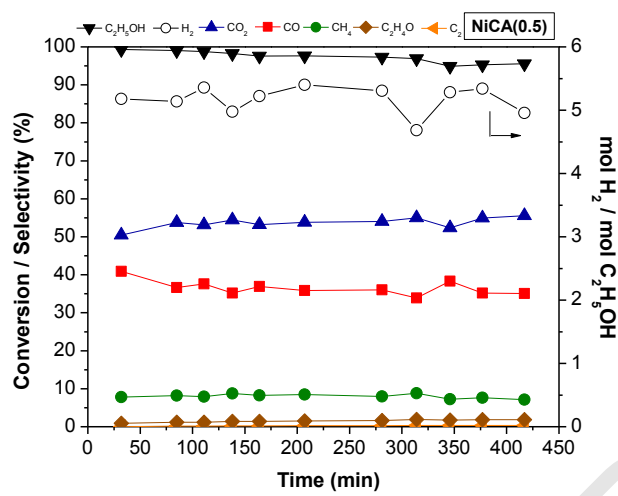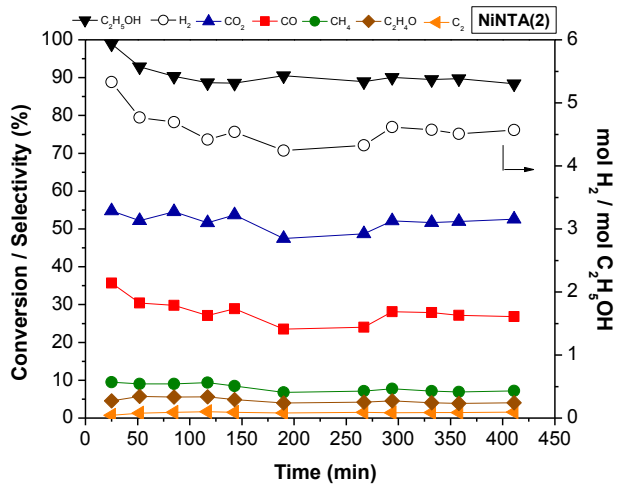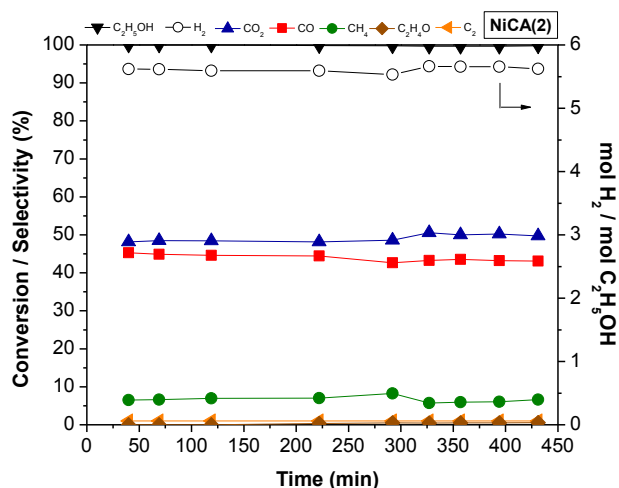
Figure 7. Ethanol conversion and product distribution in ethanol steam reforming during 7 h. T = 650 °C, S/C = 2.5, y_{C2H5OH} = 9.2 %.

3.5. Spent catalysts

The diffraction patterns of used catalysts are shown in Figure 8. $MgAl_2O_4$, CeO_2, NiO and Ni^0 phases are detected. The spinel and ceria are stable under the reaction conditions. The characteristic peak at $2\theta = 51.8°$ belonging to Ni^0 is clearly detected, showing that the systems remained active during the reaction time. This peak remains broad indicating that the nickel crystallites are nano-sized even under reaction conditions. However, it is not possible to dismiss a slight sintering of the active phase. The presence of residual NiO is also observed in $2\theta = 43.1°$ mainly in NiNTA(0.5), NiNTA(2) and NiCA(1) systems as a consequence of incomplete reduction, although no reoxidation of the active phase is ruled out. The intensity of this peak is lower than that observed in fresh samples (Figure S5), suggesting that the reduction has continued under the reactive atmosphere. NiNTA(1), NiCA(0.5) and NiCA(2) reveal less residual amount of NiO, which would indicate that these systems would have Ni^{2+} species easier to be reduced. The intensity of the characteristic graphitic carbon peak at $2\theta = 26°$ is higher for the NiL(0), NiNTA(0.5), NiNTA(2) and for NiCA(x>0) systems and it is almost undetectable to the NiNTA(1) system.
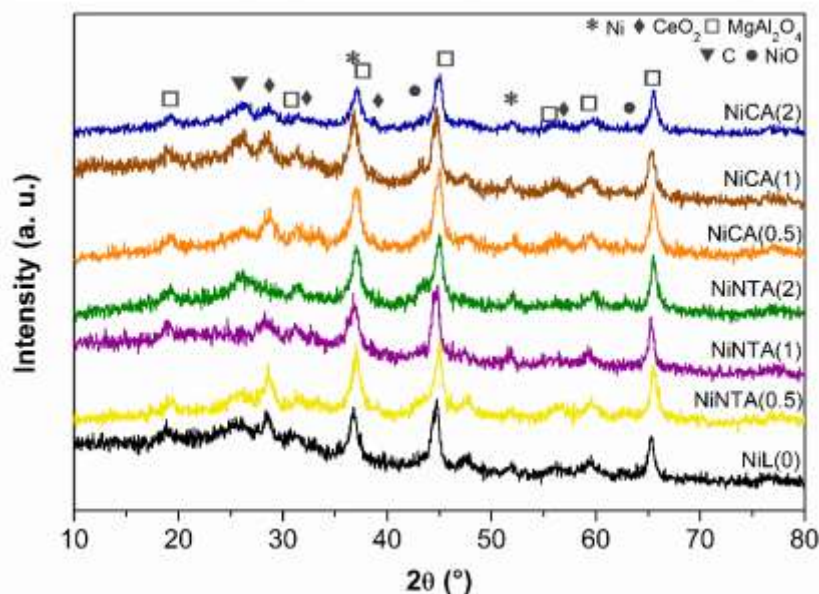
Figure 8. XRD patterns of spent catalysts after 7 h of ethanol steam reforming.

The thermograms of the catalysts used are shown in Figure S8. The weight loss of the samples under an oxidizing atmosphere mostly corresponds to the combustion of carbon deposits formed during the reforming reaction. It can be observed that the NiNTA(1) system has a small weight loss of about 2%, in agreement with those observed by XRD, Table 6. The other NTA catalysts show 32 and 35 carbon % for the NTA/Ni ratios of 0.5 and 2, respectively. The NiNTA(1) system showed larger Ni crystallite sizes than the other ones but small CeO_2 crystallite size, which enhances its oxygen release and storage properties [29] and this would allow a cooperative work with Ni^0. In addition, it has a high Ce^{3+}/Ce^{4+} surface ratio and the highest Ce/Ni^0 ratio, Table 5. The properties of ceria nanoparticles on this catalyst could explain the high removal carbon capacity during ESR. The smaller crystallite size of ceria promotes a high oxygen vacancy and mobility that would directly contribute with the gasification of carbon. The high Ce^{3+}/Ce^{4+} ratio would be related with more oxygen vacancy. Wang et al. indicated that small ceria nanoparticles promote a better performance in gasification of formaldehyde at 250 °C [77] and this was attributed to the presence of more oxygen vacancy in the ceria nanoparticles, with a crystalline size less than 5 nm. In the NiNTA(0.5) system, the amount of carbon can be attributed to differences in the degree of interaction between phases Ni and CeO_2, and partially related to the metal particle size. The reduced NiNTA(0.5) system presented the largest crystallite size of CeO_2 (Table 3) and low Ce^{3+}/Ce^{4+} and Ce/Ni^0. In addition, the XRD for the NiNTA(0.5) and NiNTA(2) systems reveal the presence of residual NiO, which would affect their performance in the reaction under the operation conditions used in this work. Maximum combustion temperatures of carbon deposits are lower in NTA-prepared catalysts, Table 6. Lower combustion temperatures are advantageous when considering catalyst regeneration procedures. For the NiNTA(1) system, the temperature decrease is higher than 100 °C.

In the CA-prepared systems the percentage of carbon deposited is similar in all the samples. The NiCA(x>0) samples have similar properties, the main differences are related to the XPS surface ratios

(Ce^{3+}/Ce^{4+} and Ce/Ni^0 ratio), Table 5. However, differences in combustion temperature are observed, associated with graphitization degree of carbon deposits. This would allow the use of a lower temperature (in the order of 50 °C less) when implementing a regeneration strategy.

Table 6. Carbon amount and maximum combustion temperature from TGA-TPO of catalysts after 7 h in reaction.

Sample	T_{max} (°C)	%C	mgC $g_{cat}^{-1}h^{-1}$
NiL(0)	702	22	30.6
NiNTA(0.5)	633	32	45.6
NiNTA(1)	537	~ 2	~ 1.4
NiNTA(2)	630	35	47.3
NiCA(0.5)	644	20	28.6
NiCA(1)	639	29	37.4
NiCA(2)	653	28	37.7

The Raman spectra of NiNTA(x) and NiCA(x) systems are shown in Figure 9. The Raman spectra of the first-order region correspond to carbonaceous zone on the catalysts [78]. These spectra were deconvolutioned in five contributions according to what has been reported by Sadezky et al. [79]. The deconvolution of the spectra was performed using Lorentzian curves for G, D1, D2 and D4 contributions and using Gaussian curve for D3 contribution. The G band around 1580 cm^{-1} is associated with the E_{2g} optical mode of graphite or sp^2 carbon materials [80]. The D bands are characteristic of disordered graphite and their intensity relative to the G band increase with a rising degree of disorder in the graphitic structure [79]. The D1 band around 1340 cm^{-1} corresponds to a graphitic lattice vibration mode with A_{1g} symmetry [79]. The I_{D1}/I_G ratio increases with the amount of disorder [81]. The band positions and Raman ratios are shown in Table 7. The I_{D1}/I_G intensity ratio were higher for the NiNTA(x) and NiCA(x) systems. Then, it could be inferred that the use of chelating agents (NTA or CA) increases the amount of disorder on the carbonaceous deposits, and it is also related to decrease in the combustion temperature, Table 6, indicating that the carbon with a major disorder burns at less temperature. A shift in G band positions is observed when NTA or CA were used in the catalyst preparation, suggesting smaller crystallite sizes of the formed graphite-like carbon [82].
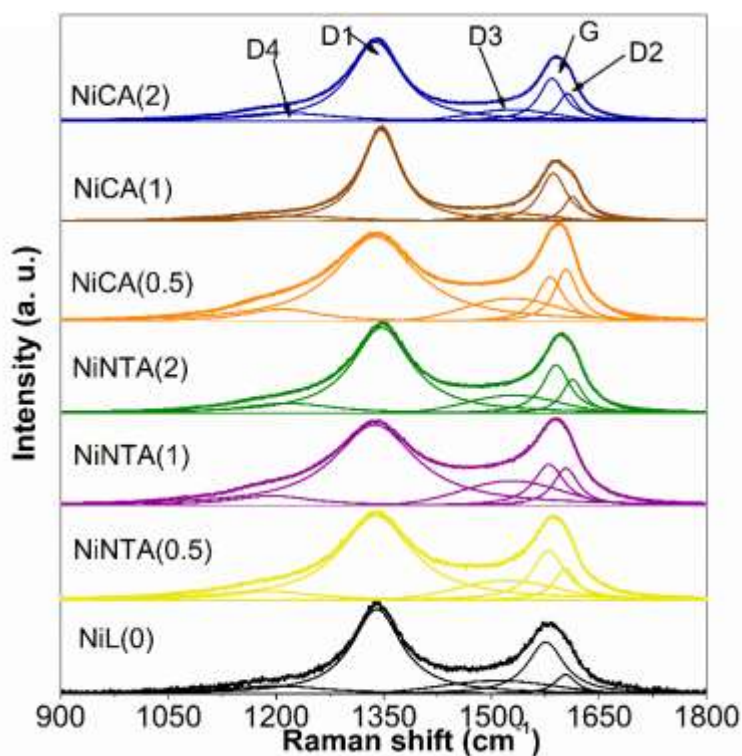
Figure 9. Raman spectra of used catalysts after 7 h in ethanol steam reforming.

The carbon deposition was also examined by SEM. All SEM images of the catalysts show two zones, Figure S9: (i) one with almost negligible amount of carbon deposits and (ii) other with an abundant deposition of carbon [83-85]. This clearly reveals that carbon deposition is not homogeneous regardless of the precursor used in the synthesis of catalysts. SEM images of NiNTA(0.5) and NiNTA(2) show zones with an abundant amount of filaments of different sizes and carbon free regions. For NiNTA(1), the carbon deposits appear to be amorphous carbon type, in agreement with the high I_{D3}/I_G ratio, Table 7 [79]. The I_{D3}/I_G ratios for NiCA(x>0) systems are also high, however only filamentous-type carbon deposits were observed by SEM. For NiCA(1) catalyst, the carbon filaments seem to be longer. The carbon type is also related to the presence of secondary products.

Nickel signal is clearly detected by EDX in the carbon regions for all catalysts, which allows to infer that the metal particle could be at the end of the filaments, which is very common in nickel catalysts. The presence of areas with and without carbon makes it possible to assume that deposition is associated with the presence of metal particles and that the bare support does not mostly contribute to the deposition mechanism or the occurrence of secondary reactions.

4. Conclusions

The catalytic performance of a series of Ni/MgAl$_2$O$_4$-CeO$_2$ catalysts were tested in ethanol steam reforming reaction. The catalysts were prepared by the wet impregnation method using L: NTA or CA as chelating agents. The influence of different L/Ni molar ratios was studied.

In all dried samples the presence of some complex species L-Ni on the support surface was verified. However, in the calcined samples, Ni^{2+} species were in an octahedral environment similar to NiO without a significant amount of carbon residues from the chelating agent. The changes in surface properties of catalysts were associated to a memory effect.

Improved interactions among NiO-CeO$_2$ and Ni-CeO$_2$ were obtained by the use of chelating agents. These interactions were revealed by HRTEM images, the behaviour under reduction conditions and the increase in the Ce/Ni^0 surface ratio.

The NTA addition in the preparation of catalytic systems allowed to decrease the NiO crystallite sizes. After reduction, the Ni^0 crystallite sizes were smaller for NiNTA(0.5) and NiNTA(2) systems. Due to the redissolution of the ceria during impregnation with solutions containing Ni^{2+} and NTA, the crystallite size of CeO$_2$ was also affected, mainly with a molar ratio NTA/Ni =1 and 2.

The CA addition in the preparation of Ni catalysts promoted the formation of smaller NiO and Ni^0 crystallite sizes, with a slight effect on the size of CeO$_2$ particles.

The catalysts prepared with a molar ratio NTA/Ni=1 and CA/Ni=2 exhibited better catalytic performances in the ethanol reforming reaction under the operation conditions used. The NiNTA(1) and NiCA(2) system presented high Ce/Ni^0 surface ratios. The NiNTA(1) showed a high tolerance to carbon deposition while no improvement in tolerance to carbon deposition was observed for NiCA(2). The use of chelating agents in catalysts preparation induced changes in the type of carbon. The carbon removal through oxidation in catalysts prepared using NTA or CA requires lower temperatures, which is beneficial for implementing a regeneration strategy. Although, all the NiL(x) systems showed a good catalytic performance in ethanol steam reforming, under the experimental conditions used, the best performance in terms of hydrogen production were obtained with NiNTA(1) and NiCA(2) systems. These systems were prepared using the stoichiometric molar ratios to form the most stable complex in solution between nickel and chelating agent.

CRediT authorship contribution statement

Alejandra C. Villagran-Olivares: Investigation, Formal analysis, Writing – original draft, Visualization. **Mariana N. Barroso**: Conceptualization, Validation. **Carlos A. López**: Formal analysis, Validation. **Jordi Llorca**: Validation. **María C. Abello**: Conceptualization, Validation, Visualization, Writing - review & editing.

Declaration of Competing Interest

The authors declare that they have no known competing financial interests or personal relationships that could have appeared to influence the work reported in this paper.

Acknowledgments

References

[1]   S. Ogo, Y. Sekine, Recent progress in ethanol steam reforming using non-noble transition metal catalysts: A review, Fuel Process. Technol. 199 (2020) 106238, https://doi.org/10.1016/j.fuproc.2019.106238.

[2]   Q. Zhang, K. Long, J. Wang, T. Zhang, Z. Song, Q. Lin, A novel promoting effect of chelating ligand on the dispersion of Ni species over Ni/SBA-15 catalyst for dry reforming of methane, Int. J. Hydrog. Energy 42 (2017) 14103-14114, https://doi.org/10.1016/j.ijhydene.2017.04.090.

[3]   J.L. Contreras, J. Salmones, J.A. Colín-Luna, L. Nuño, B. Quintana, I. Córdova, B. Zeifert, C. Tapia, G.A. Fuentes, Catalysts for H2 production using the ethanol steam reforming (a review), Int. J. Hydrog. Energy 39 (2014) 18835, https://doi.org/10.1016/j.ijhydene.2014.08.072.

[4]   S. Bepari, D. Kuila, Steam reforming of methanol, ethanol and glycerol over nickel-based catalysts-A review, Int. J. of Hydrog. Energy 45 (2020) 18090-18113, https://doi.org/10.1016/j.ijhydene.2019.08.003.

[5]   C. Montero, A. Remiro, B. Valle, L. Oar-Arteta, J. Bilbao, A.G. Gayubo, Origin and nature of coke in ethanol steam reforming and its role in deactivation of Ni/La2O3−αAl2O3 catalyst, Ind. Eng. Chem. Res. 58 (2019) 14736−14751, https://doi.org/10.1021/acs.iecr.9b02880.

[6]   J.R. Rostrup-Nielsen, J. Sehested, J. Nørskov, Hydrogen and synthesis gas by steam- and CO2 reforming, Adv. Catal. 47 (2002) 65-139, https://doi.org/10.1016/S0360-0564(02)47006-X.

[7]   Y.C. Sharma, A. Kumar, R. Prasad, S.N. Upadhyay, Ethanol steam reforming for hydrogen production: Latest and effective catalyst modification strategies to minimize carbonaceous deactivation, Renew. Sust. Energy Rev. 74 (2017) 89-103, https://doi.org/10.1016/j.rser.2017.02.049.

[8]   L.V. Mattos, G. Jacobs, B.H. Davis, F.B. Noronha, Production of hydrogen from ethanol: review of reaction mechanism and catalyst deactivation, Chem. Rev. 112 (2012) 4094-4123, https://doi.org/10.1021/cr2000114.

[9]   A.J. van Dillen, R. Terorde, D. Lensveld, J. Geus, K. de Jong, Synthesis of supported catalysts by impregnation and drying using aqueous chelated metal complexes, J. Catal. 216 (2003) 257-264, https://doi.org/10.1016/S0021-9517(02)00130-6.

[10]   U.C. Abubakar, K.R. Alhooshani, T.A. Saleh, Effect of ultrasonication and chelating agents on the dispersion of NiMo catalysts on carbon for Hydrodesulphurization, J. Environ. Chem. Eng. 8 (2020) 103811, https://doi.org/10.1016/j.jece.2020.103811.

[11]   J. Escobar, M.C. Barrera, J.A. de los Reyes, J.A. Toledo, V. Santes, J.A. Colin, Effect of chelating ligands on Ni–Mo impregnation over wide-pore ZrO2–TiO2, J. Mol. Catal. A: Chem. 287 (2008) 33-40, https://doi.org/10.1016/j.molcata.2008.02.022.

[12]   T. Shimizu, K. Hiroshima, T. Honma, T. Mochizuki, M. Yamada, Highly active hydrotreatment catalysts prepared with chelating agents, Catal. Today 45 (1998) 271-276, https://doi.org/10.1016/S0920-5861(98)00227-2.

[13]   T. Mochizuki, T. Hara, N. Koizumi, M. Yamada, Surface structure and Fischer–Tropsch synthesis activity of highly active Co/SiO2 catalysts prepared from the impregnating solution modified with some chelating agents, Appl. Catal. A: Gen. 317 (2007) 97-104, https://doi.org/10.1016/j.apcata.2006.10.005.

[14]   J.-S. Girardon, E. Quinet, A. Griboval-Constant, P.A. Chernavskii, L. Gengembre, A.Y. Khodakov, Cobalt dispersion, reducibility, and surface sites in promoted silica-supported Fischer–Tropsch catalysts, J. Catal. 248 (2007) 143–157, https://doi.org/10.1016/j.jcat.2007.03.002.

[15]   S. Karnjanakom, G. Guan, B. Asep, X. Dua, X. Hao, C. Samart, A. Abudula, Catalytic steam reforming of tar derived from steam gasification of sunflower stalk over ethylene glycol assisting prepared Ni/MCM-41, Energy Conv. Manag. 98 (2015) 359–368, https://doi.org/10.1016/j.enconman.2015.04.007.

[16]   X. Lu, J.-F. Chen, Y. Tan, Y. Zhang, A highly dispersed nickel supported catalyst for dry reforming of methane, Catal. Comm. 20 (2012) 6–11, https://doi.org/10.1016/j.catcom.2012.01.002.

[17]   Y. Bang, S. Park, S.-J. Han, J. Yoo, J.-H. Song, J.H. Choi, K.H. Kang, I.K. Song, Hydrogen production by steam reforming of liquefied natural gas (LNG) over mesoporous Ni/Al2O3 catalyst prepared by an EDTA-assisted impregnation method, Appl. Catal. B: Environ.180 (2016) 179-188, https://doi.org/10.1016/j.apcatb.2015.06.023.

[18]   K. Al-Dalama, B. Aravind, A. Stanislaus, Influence of complexing agents on the adsorption of molybdate and nickel ions on alumina, Appl. Catal. A: Gen. 296 (2005) 49-53, https://doi.org/10.1016/j.apcata.2005.07.041.

[19]   G. Słowik, M. Greluk, M. Rotko, A. Machocki, Evolution of the structure of unpromoted and potassium-promoted ceria-supported nickel catalysts in the steam reforming of ethanol, Appl. Catal. B: Environ. 221 (2018) 490–509, https://doi.org/10.1016/j.apcatb.2017.09.052.

[20]   C. Wu, P. T. Williams, Hydrogen production from steam reforming of ethanol with nano-Ni/SiO2 catalysts prepared at different Ni to citric acid ratios using a sol–gel method, Appl. Catal. B: Environ. 102 (2011) 251–259, https://doi.org/10.1016/j.apcatb.2010.12.005.

[21]   J. Ryczkowski, W. Grzegorczyk, D. Nazimek, Support modification with organic reagents and its influence on the development of metal active surface areas in Ni/Al2O3 catalysts, Appl. Catal. A: Gen. 126 (1995) 341-349, https://doi.org/10.1016/0926-860X(95)00032-1.

[22]   G. Anderegg, Critical survey of stability constants of NTA complexes, Pure Appl. Chem. 54 (1982) 2693-2758, https://dx.doi.org/10.1351/pac198254122693.

[23]   W. Hummel, G. Anderegg, L. Rao, I. Puigdomènech, O. Tochiyama, Chemical thermodynamics of compounds and complexes of U, Np, Pu, Am, Tc, Se, Ni and Zr with selected organic ligands, USA, Elsevier Science, 2005.

[24]   A.E. Galetti, M.F. Gomez, L.A. Arrúa, M.C. Abello, Hydrogen production by ethanol reforming over NiZnAl catalysts: Influence of Ce addition on carbon deposition, Appl. Catal. A: General 348 (2008) 94–102, https://doi.org/10.1016/j.apcata.2008.06.039.

[25]   A. Trovarelli, J. Llorca, Ceria catalysts at nanoscale: How do crystal shapes shape catalysis?, ACS Catal. 7 (2017) 4716–4735, https://doi.org/10.1021/acscatal.7b01246.

[26]   L. Soler, A. Casanovas, J. Ryan, I. Angurell, C. Escudero, V. Pérez-Dieste, J. Llorca, Dynamic reorganization of bimetallic nanoparticles under reaction depending on the support nanoshape: The case of RhPd over ceria nanocubes and nanorods under ethanol steam reforming, ACS Catal. 9 (2019) 3641–3647, https://doi.org/10.1021/acscatal.9b00463.

[27]   T. Montini, M. Melchionna, M. Monai, P. Fornasiero, Fundamentals and catalytic applications of CeO2-based materials, Chem. Rev. 116 (2016) 5987–6041, https://doi.org/10.1021/acs.chemrev.5b00603.

[28]   F. Wang, Y. Wang, L. Zhang, J. Zhu, B. Han, W. Fan, L. Xu, H. Yu, W. Cai, Z. Li, Z. Deng, W. Shi, Performance enhancement of methane dry reforming reaction for syngas production over Ir/Ce0.9La0.1O2-nanorods catalysts, Catal. Today 355 (2020) 502-511, https://doi.org/10.1016/j.cattod.2019.06.067.

[29]   A. Elmhamdi, R. Castañeda, A. Kubacka, K. Nahdi, A. Martínez, Characterization and catalytic properties of CuO/CeO2/MgAl2O4 for preferential oxidation of CO in H2-rich streams, Appl. Catal. B: Environ. 188 (2016) 292-304, https://doi.org/10.1016/j.apcatb.2016.02.011.

[30]   A.C. Villagrán-Olivares, M.F. Gomez, M.N. Barroso, M.C. Abello, Hydrogen production from ethanol: Synthesis of Ni catalysts assisted by chelating agents, Mol. Catal. 481 (2020) 110164, https://doi.org/10.1016/j.mcat.2018.08.006.

[31]   A.C. Villagrán-Olivares, M. F. Gomez, C. López, M.N. Barroso, M.C. Abello, Effect of EDTA in preparation of Ni catalysts toward a carbon-resistant ethanol reforming, Appl. Catal. B: Environ. 264 (2020) 118510, https://doi.org/10.1016/j.apcatb.2019.118510.

[32]   B.A.T. Mehrabadi, S. Eskandari, U. Khan, R.D. White, J.R. Regalbuto, Adv. Catal. 61 (2017) 1-35, A review of preparation methods for supported metal catalysts, https://doi.org/10.1016/bs.acat.2017.10.001.

[33]   F. Wang, K. Han, L. Xu, H. Yu, W. Shi, Ni/SiO2 catalyst prepared by strong electrostatic adsorption for a low-temperature methane dry reforming reaction, Ind. Eng. Chem. Res. 60 (2021) 3324−3333, https://dx.doi.org/10.1021/acs.iecr.0c06020.

[34]   H.M. Rietveld, A profile refinement method for nuclear and magnetic structures, J. Appl. Crystallogr. 2 (1969) 65–71, https://doi.org/10.1107/S0021889869006558.

[35]   J. Rodríguez-Carvajal, Recent advances in magnetic structure determination by neutron powder diffraction, Phys. B Condens. Matter 192 (1993) 55–69, https://doi.org/10.1016/0921-4526(93)90108-I.

[36]   P. Thompson, D.E. Cox, J.B. Hastings, Rietveld refinement of Debye–Scherrer synchrotron X-ray data from Al2O3, J. Appl. Crystallogr. 20 (1987) 79–83, https://doi.org/10.1107/S0021889887087090.

[37]   J.R.H. Ross, Chapter 5 - Catalyst Characterization, Ed.: J.R.H. Ross, Contemporary Catalysis, Elsevier, (2019), pages 121-132, ISBN 9780444634740, https://doi.org/10.1016/b978-0-444-63474-0.00005-9.

[38]   I. Puigdomenech, Medusa software, Chem. Equilibr. Diagrams 2 (2013), https://www.kth.se/en/che/medusa/downloads-1.386254.

[39]   L. Bonneviot, O. Legendre, M. Kermarec, D. Olivier, M. Che, Characterization by UV-vis-NIR reflectance spectroscopy of the exchange sites of nickel on silica, J. Colloid Interf. Sci. 134 (1990) 534-547, https://doi.org/10.1016/0021-9797(90)90161-G.

[40]   G. George, S. Anandhan, Synthesis and characterisation of nickel oxide nanofibre webs with alcohol sensing characteristics, RSC Adv. 4 (2014) 62009–62020, https://doi.org/10.1039/C4RA11083H.

[41]   V.A. Suárez-Toriello, C.E. Santolalla-Vargas, J.A. de los Reyes, A. Vázquez-Zavala, M. Vrinat, C. Geantet, Influence of the solution pH in impregnation with citric acid and activity of Ni/W/Al2O3 catalysts, J. Mol. Catal. A: Chem. 404–405 (2015) 36–46, https://doi.org/10.1016/j.molcata.2015.04.005.

[42]   J. Calvache-Muñoz, F.A. Prado, J.E. Rodríguez-Páez, Cerium oxide nanoparticles: Synthesis, characterization and tentative mechanism of particle formation, Colloids Surf. A: Physicochem. Eng. Asp. 529 (2017) 146-159, https://doi.org/10.1016/j.colsurfa.2017.05.059.

[43]   Z. Yu, X. Hu, P. Jia, Z. Zhang, D. Dong, G. Hu, S. Hu, Y. Wang, J. Xiang, Steam reforming of acetic acid over nickel-based catalysts: The intrinsic effects of nickel precursors on behaviors of nickel catalysts, Appl. Catal. B: Environ. 237 (2018) 538–553, https://doi.org/10.1016/j.apcatb.2018.06.020.

[44]   K.-Q. Sun, E. Marceau, M. Che, Evolution of nickel speciation during preparation of Ni–SiO2 catalysts: effect of the number of chelating ligands in [Ni(en)x(H2O)6−2x]2+ precursor complexes, Phys. Chem. Chem. Phys. 8 (2006) 1731-1738, https://doi.org/10.1039/B513319J.

[45]   R.A. Ortega-Domínguez, H. Vargas-Villagrán, C. Peñaloza-Orta, K. Saavedra-Rubio, X. Bokhimi, T.E. Klimova, A facile method to increase metal dispersion and hydrogenation activity of Ni/SBA-15 catalysts, Fuel 198 (2017) 110–122, https://doi.org/10.1016/j.fuel.2016.12.037.

[46]   N. Koizumi, Y. Ibi, D. Hongo, Y. Hamabe, S. Suzuki, Y. Hayasaka, T. Shindo, M. Yamada, Mechanistic aspects of the role of chelating agents in enhancing Fischer–Tropsch synthesis activity of Co/SiO2 catalyst: Importance of specific interaction of Co with chelate complex during calcination, J. Catal. 289 (2012) 151-163, https://doi.org/10.1016/j.jcat.2012.02.003.

[47]   L. Espinosa-Alonso, K.P. de Jong, B.M. Weckhuysen, Effect of the nickel precursor on the impregnation and drying of γ-Al2O3 catalyst bodies: A UV−vis and IR microspectroscopic study, J. Phys. Chem. C 112 (2008) 7201-7209, https://doi.org/10.1021/jp710676v.

[48]   L.Y. Wang, G.Q. Wu, D.G. Evans, Synthesis and characterization of a layered double hydroxide containing an intercalated nickel(II) citrate complex, Mater. Chem. Phys. 104 (2007) 133-140, https://doi.org/10.1016/j.matchemphys.2007.02.098.

[49]   S. Bepari, S. Basu, N. Pradhan, A.K. Dalai, Steam reforming of ethanol over cerium-promoted Ni-Mg-Al hydrotalcite catalysts, Catal. Today 291 (2017) 47-57, https://doi.org/10.1016/j.cattod.2017.01.027.

[50]   G. Sócrates; Infrared and Raman Characteristic Group Frequencies: Tables and Charts. 3rd Edition, J. Wiley and Sons, 2001. ISBN: 0-471-85298-8.

[51]   O. Gyliene, J. Aikaite, O. Nivinskiene, Recycling of Ni(II)–citrate complexes using precipitation in alkaline solutions, J. Hazard Mater. 109 (2004) 105-111, https://doi.org/10.1016/j.jhazmat.2004.03.008.

[52]   K.A. Tarasov, D. O´Hare, V. P. Isupov, Solid-state chelation of metal ions by ethylenediaminetetraacetate intercalated in a layered double hydroxide, Inorg. Chem. 42 (2003) 1919-1927, https://doi.org/10.1021/ic0203926.

[53]   F. Wypych, G.G. Carbajal Arízaga, J.E. Ferreira da Costa Gardolinski, Intercalation and functionalization of zinc hydroxide nitrate with mono- and dicarboxylic acids, J. Colloid Interf. Sci. 283 (2005) 130–138, https://doi.org/10.1016/j.jcis.2004.08.125.

[54]   W. Brockner, C. Ehrhardt, M. Gjikaj, Thermal decomposition of nickel nitrate hexahydrate, Ni(NO3)2•6H2O, in comparison to Co(NO3)2•6H2O and Ca(NO3)2•4H2O, Thermochim. Acta 456 (2007) 64–68, https://doi.org/10.1016/j.tca.2007.01.031.

[55]   G. Leofanti, M. Padovan, G. Tozzola, B. Venturelli, Surface area and pore texture of catalysts, Catal. Today 41 (1998) 207-219, https://doi.org/10.1016/S0920-5861(98)00050-9.

[56]   S.A. Theofanidis, V.V. Galvita, H. Poelman, R. Batchu, L.C. Buelens, C. Detavernier, G.B. Marin, Mechanism of carbon deposits removal from supported Ni catalysts, Appl. Catal. B: Environ. 239 (2018) 502-512, https://doi.org/10.1016/j.apcatb.2018.08.042.

[57]   M. Zarei, F. Meshkani, M. Rezaei, Preparation of mesoporous nanocrystalline Ni-MgAl2O4 catalysts by sol-gel combustion method and its applications in dry reforming reaction, Adv. Powder Technol. 27 (2016) 1963–1970, https://doi.org/10.1016/j.apt.2016.06.028.

[58] C.E. Santolalla-Vargas, V.A. Suárez Toriello, J.A. de los Reyes, D.K. Cromwell, B. Pawelec, J.L.G. Fierro, Effects of pH and chelating agent on the NiWS phase formation in NiW/γ-Al2O3 HDS catalysts, Mater. Chem. Phys. 166 (2015) 105-115, https://doi.org/10.1016/j.matchemphys.2015.09.033.

[59] K.Y. Koo, S.-h. Lee, U.H. Jung, H.-S. Roh, W.L. Yoon, Syngas production via combined steam and carbon dioxide reforming of methane over Ni–Ce/MgAl2O4 catalysts with enhanced coke resistance, Fuel Process. Technol. 119 (2014) 151-157, https://doi.org/10.1016/j.fuproc.2013.11.005.

[60] B. Li, X. Qian, X. Wang, Oxidative CO2 reforming of methane over stable and active nickel-based catalysts modified with organic agents, Int. J. Hydrog. Energy 40 (2015) 8081-8092, https://doi.org/10.1016/j.ijhydene.2015.04.104.

[61] R. Jalali, B. Nematollahi, M. Rezaei, M. Baghalha, Mesoporous nanostructured Ni/MgAl2O4 catalysts: Highly active and stable catalysts for syngas production in combined dry reforming and partial oxidation, Int. J. Hydrog. Energy 44 (2019) 10427-10442, https://doi.org/10.1016/j.ijhydene.2018.12.186.

[62] S. Damyanova, B. Pawelec, R. Palcheva, Y. Karakirova, M.C. Capel Sanchez, G. Tyuliev, E. Gaigneaux, J.L.G. Fierro, Structure and surface properties of ceria-modified Ni-based catalysts for hydrogen production, Appl. Catal. B: Environ. 225 (2018) 340-353, https://doi.org/10.1016/j.apcatb.2017.12.002.

[63] J.A. Santander, G.M. Tonetto, M.N. Pedernera, E. López, Ni/CeO2–MgO catalysts supported on stainless steel plates for ethanol steam reforming, Int. J. Hydrog. Energy 42 (2017) 9482-9492, https://doi.org/10.1016/j.ijhydene.2017.03.169.

[64] A. Ebadi, S. Tourani, F. Khorasheh, Synthesis of highly dispersed nanosized NiO/MgO-Al2O3 catalyst for the production of synthetic natural gas with enhanced activity and resistance to coke Formation, Ind. Eng. Chem. Res. 57 (2018) 12700−12714, https://doi.org/10.1021/acs.iecr.8b01878.

[65] A. Di Michele, A. Dell'Angelo, A. Tripodi, E. Bahadori, F. Sánchez, D. Motta, N. Dimitratos, I. Rossetti, G. Ramis, Steam reforming of ethanol over Ni/MgAl2O4 catalysts, Int. J. Hydrog. Energy 44 (2019) 952-964, https://doi.org/10.1016/j.ijhydene.2018.11.048.

[66] M. Li, X. Wang, S. Li, S. Wang, X. Ma, Hydrogen production from ethanol steam reforming over nickel based catalyst derived from Ni/Mg/Al hydrotalcite-like compounds, Int. J. Hydrog. Energy 35 (2010) 6699-6708, https://doi.org/10.1016/j.ijhydene.2010.04.105.

[67] M. Chen, Y. Wang, Z. Yang, T. Liang, S. Liu, Z. Zhou, X. Li, Effect of Mg-modified mesoporous Ni/Attapulgite catalysts on catalytic performance and resistance to carbon deposition for ethanol steam reforming, Fuel 220 (2018) 32–46, https://doi.org/10.1016/j.fuel.2018.02.013.

[68] S.C.M. Mizuno, A.H. Braga, C.E. Hori, J.B.O. Santos, J.M.C. Bueno, Steam reforming of acetic acid over MgAl2O4-supported Co and Ni catalysts: Effect of the composition of Ni/Co and reactants on reaction pathways, Catal. Today 296 (2017) 144–153, https://doi.org/10.1016/j.cattod.2017.04.023.

[69] L. Jalowiecki-Duhamel, C. Pirez, M. Capron, F. Dumeignil, E. Payen, Hydrogen production from ethanol steam reforming over cerium and nickel based oxyhydrides, Int. J. Hydrog. Energy 35 (2010) 12741-12750, https://doi.org/10.1016/j.ijhydene.2009.08.080.

[70] R. Yang, X. Li, J. Wu, X. Zhang, Z. Zhang, Y. Cheng, J. Guo, Hydrotreating of crude 2-ethylhexanol over Ni/Al2O3 catalysts: Surface Ni species-catalytic activity correlation, Appl. Catal. A: Gen. 368 (2009) 105-112, https://doi.org/10.1016/j.apcata.2009.08.021.

[71] K. Han, W. Yu, L. Xu, Z. Deng, H. Yu, F. Wang, Reducing carbon deposition and enhancing reaction stability by ceria for methane dry reforming over Ni@SiO2@CeO2 catalyst, Fuel 291 (2021) 120182, https://doi.org/10.1016/j.fuel.2021.120182.

[72]   A. Iriondo, V.L. Barrio, J.F. Cambra, P.L. Arias, M.B. Guemez, M.C. Sanchez-Sanchez, R.M. Navarro, J.L.G. Fierro, Glycerol steam reforming over Ni catalysts supported on ceria and ceria-promoted alumina, Int. J. of Hydrog. Energy 35 (2010) 11622-11633, https://doi.org/10.1016/j.ijhydene.2010.05.105.

[73]   E. Varga, Z. Ferencz, A. Oszkó, A. Erdőhelyi, J. Kiss, Oxidation states of active catalytic centers in ethanol steam reforming reaction on ceria based Rh promoted Co catalysts: An XPS study, J. Mol. Catal A: Chem. 397 (2015) 127-133, https://doi.org/10.1016/j.molcata.2014.11.010.

[74]   J.W.C. Liberatori, R.U. Ribeiro, D. Zanchet, F.B. Noronha, J.M.C. Bueno, Steam reforming of ethanol on supported nickel catalysts, Appl. Catal. A: Gen. 327 (2007) 197-204, https://doi.org/10.1016/j.apcata.2007.05.010.

[75]   J. Chen, D. Xu, Hydrogen production by the steam reforming of bio-ethanol over nickel-based catalysts for fuel cell applications, Int. J. Sustain. Green Energy 6 (2017) 28-38. https://doi.org/10.11648/j.ijrse.20170603.11.

[76]   F. Haga, T. Nakajima, H. Miya, S. Mishima, Catalytic properties of supported cobalt catalysts for steam reforming of ethanol, Catal. Lett. 48 (1997) 223-227, https://doi.org/10.1023/A:1019039407126.

[77]   Y. Wang, F. Wang, K. Han, W. Shi and H. Yu, Ultra-small CeO2 nanoparticles supported on SiO2 for indoor formaldehyde oxidation at low temperature, Catal. Sci. Technol. 10 (2020) 6701-6712, https://doi.org/10.1039/D0CY00988A.

[78]   M. Pawlyta, J.-N. Rouzaud, S. Duber, Raman microspectroscopy characterization of carbon blacks: Spectral analysis and structural information, Carbon 84 (2015) 479-490, https://doi.org/10.1016/j.carbon.2014.12.030.

[79]   A. Sadezky, H. Muckenhuber, H. Grothe, R. Niessner, U. Pöschl, Raman microspectroscopy of soot and related carbonaceous materials: Spectral analysis and structural information, Carbon 43 (2005) 1731–1742, https://doi.org/10.1016/j.carbon.2005.02.018.

[80]   J. McGregor, Z. Huang, E.P.J. Parrott, J.A. Zeitler, K.L. Nguyen, J.M. Rawson, A. Carley, T.W. Hansen, J.-P. Tessonnier, D.S. Su, D. Teschner, E.M. Vass, A. Knop-Gericke, R. Schlögl, L.F. Gladden, Active coke: Carbonaceous materials as catalysts for alkane dehydrogenation, J. Catal. 269 (2010) 329–339, https://doi.org/10.1016/j.jcat.2009.11.016.

[81]   L. Bokobza, J.-L. Bruneel, M. Couzi, Raman spectra of carbon-based materials (from graphite to carbon black) and of some silicone composites, Carbon 1 (2015) 77-94, https://doi.org/10.3390/c1010077.

[82]   H.-Z. Wang, L.-L. Sun, Z.-J. Sui, Y.-A. Zhu, G.-H. Ye, D. Chen, X.-G. Zhou, W.-K. Yuan, Coke formation on Pt–Sn/Al2O3 catalyst for propane dehydrogenation, Ind. Eng. Chem. Res. 57 (2018) 8647-8654, https://doi.org/10.1021/acs.iecr.8b01313.

[83]   A.C. Villagrán Olivares, M.N. Barroso, M.F. Gomez, M.C. Abello, Ni-supported catalysts for ethanol steam reforming: effect of the solvent and metallic precursor in catalyst preparation, Int. J. Ind. Chem. 9 (2018) 61-73, https://doi.org/10.1007/s40090-018-0135-6.

[84]   M.N. Barroso, M.F. Gomez, L.A. Arrúa, M.C. Abello, Co catalysts modified by rare earths (La, Ce or Pr) for hydrogen production from ethanol, Int. J. Hydrog. Energy 39 (2014) 8712-8719, https://doi.org/10.1016/j.ijhydene.2013.12.043.

[85]   A.E. Galetti, M.F. Gomez, L.A. Arrúa, M.C. Abello, Ethanol steam reforming over Ni/ZnAl2O4-CeO2. Influence of calcination atmosphere and nature of catalytic precursor, Appl. Catal. A: Gen. 408 (2011) 78– 86, https://doi.org/10.1016/j.apcata.2011.09.006.

Figure Captions

Figure 1. UV-Vis spectra of impregnation solutions (A) and DR UV-Vis-NIR spectra of dried catalysts (B).

Figure 2. Infrared spectra of dried catalysts.

Figure 3. XRD patterns of reduced catalysts.

Figure 4. TPR profiles of fresh catalysts.

Figure 5. XPS spectra of reduced catalysts.

Figure 6. HRTEM images of reduced catalysts.

Figure 7. Ethanol conversion and product distribution in ethanol steam reforming during 7 h. T = 650 °C, S/C = 2.5, y_{C2H5OH} = 9.2 %.

Figure 8. XRD patterns of spent catalysts after 7 h of ethanol steam reforming.

Figure 9. Raman spectra of used catalysts after 7 h in ethanol steam reforming.